A hybrid analytical-FEM 3D approach including wear effects to simulate fretting fatigue endurance : application to steel wires in crossed contact

Sébastien Montalvo, Siegfried Fouvry, Michaël Martinez

Sébastien Montalvo, Siegfried Fouvry, Michaël Martinez, A hybrid analytical-FEM 3D approach including wear effects to simulate fretting fatigue endurance: Application to steel wires in crossed contact, Tribology International 187 (2023) 108713
(https://doi.org/10.1016/j.triboint.2023.108713)

A hybrid analytical-FEM 3D approach including wear effects to simulate fretting fatigue endurance: application to steel wires in crossed contact

Authors:

Sébastien Montalvo [a,b], Siegfried Fouvry [a], Michaël Martinez [b]

[a] Laboratoire de Tribologie et de Dynamique des Systèmes, Centrale Lyon, 36 Av. Guy de Collongue, 69134 Écully, France

[b] IFP Energies nouvelles, Rond point de l'échangeur de Solaize, 69360 Solaize, France

Keywords:

Wear modelling, FEM, fretting fatigue, steel wires

Abstract

Fretting fatigue causes failures in steel wire ropes. A crossed wires set-up was used to investigate the influence of displacement amplitude on fretting fatigue damage. The analysis confirms previous literature results, showing a beneficial effect of wear in gross slip regime, which extends the contact area and thus decreases the contact stresses. The computation of such combined cracking and wear processes is very expensive using a classical FEM strategy, particularly for 3D contact geometries. To palliate such limitations, a hybrid analytical-numerical strategy was developped. It consists in estimating pressure and shear stress surface fields using analytical formulations, then to transpose these fields to an FEM model. This allows to simulate contact geometry modifications in a fast and efficient way.

Nomenclature

P contact normal force

Q^* contact tangential force amplitude

μ_{GS} friction coefficient in gross slip regime for the crossed wires contact

μ_t friction coefficient at the partial to gross slip transition for the crossed wires contact

p pressure field

q shear stress field

a_X semi-major axe of the fretting scar ellipse

a_Y semi-minor axe of the fretting scar ellipse

σ fatigue stress

σ_a fatigue stress amplitude

σ_m mean fatigue stress

δ^*_{FA} displacement amplitude of the fretting actuator

$\delta^*_{FA,0}$ displacement amplitude of the specimen at the contacting point

δ^* effective displacement amplitude

δ^*_t effective displacement amplitude at the partial slip/gross slip transition

δ^*_s sliding amplitude

N_c number of cycles

N_f number of cycles to failure

σ_D fatigue limit in pure alternated tension

σ_{SWT} Smith-Watson-Topper equivalent stress

ℓ_d critical distance

σ_{SWT,ℓ_d} Smith-Watson-Topper equivalent stress evaluated at the critical distance under the hotspot

1. Introduction

Spiral strand steel wire ropes are composed of steel wires helically wound around a central wire in successive layers. Two successive layers are usually laid in opposite directions, producing punctual contacts between the wires. Fretting is defined as a cyclic relative movement of very small amplitude between two bodies in contact. The resulting high local stresses under the contact interface can lead to crack initiation. If only a fretting load is imposed, cracks do not

propagate deeply, as the contact stresses decrease rapidly below the surface. When fretting is combined with fatigue loads, inducing fretting fatigue, the cracks may propagate, inducing failure. This phenomenon is considered one of the main causes of damage in steel ropes [1], and has been widely studied [2–5] Raoof et al. have shown in various publications[6–9] that fretting fatigue damage at the punctual contacts is the main factor controlling the rope fatigue life. Understanding and quantifying the phenomena responsible for this degradation is essential to design reliable ropes. When the stress fields in the solids are known, multiaxial fatigue criteria can be used to predict crack nucleation. These stress fields are often calculated numerically.

One of the key issues in these simulations is wear modelling, as wear continously modifies the geometry of the solids in contact. This induces contact stress field modifications which have to be considered for accurate cracking failure predictions. The strategy employed by several researchers [10–12] is to continuously adapt the mesh of the FEM model, displacing the nodes. Madge et al [13] applied this approach to predict fretting fatigue lifetime: they created a wear model based on Archard's law, combined with a SWT (Smith-Watson-Topper) cumulative damage analysis. Arnaud et al [14] modelled the debris layer for improved lifetime predictions. However, these methods are very computationally expensive, which considerably restricts their application. Another solution is to use semi-analytical models : Gallego and Nélias [15] created a semi-analytical wear model, based on the integration of Boussinesq and Cerruti potentials, which is fast enough for 3D analyses. This model was extended by Done et al [16] then by Garcin et al [17] to take into account the debris layer.

In this paper, we present another wear modelling strategy : instead of simulating wear using a fully coupled FEM analysis, we analytically estimate the pressure and shear fields, taking into account the surface wear, then transpose these contact fields to an FEM specimen. This approach stemmed from the need to efficiently model fretting fatigue damage of steel wires in crossed contact while taking into account contact geometry modification. This approach combines the versatily and ease of application of a FEM analysis with the low numerical cost of an analytical determination of the pressure and shear fields. This comes at the expense of some precision compared to the semi-analytical or full FEM methods. This hybrid method is intended as a simpler and faster mean of estimating the crack initiation risk in fretting fatigue. The reliability of this hybrid analytical-FEM numerical strategy will be evaluated by comparing the predictions of dedicated steel crossed fretting fatigue experiments from partial to gross slip conditions taking into the contact geometry modifications induced by surface wear damages.

2. Materials and methods

2.1. Materials

The tested specimens are high strength steel wires with a 4.85 mm diameter manufactured through wire drawing. The wires are initially coated with a 50 µm zinc layer which was systematically removed using inhibited hydrochloric acid. This chemical attack leaves the steel intact. Static traction and fatigue tests were conducted on specimens machined from the wires. The material properties of the steel are listed in Table 1.

Table 1 : material properties of the steel

Elasticity modulus E	210 000 MPa
Yield stress	1800 MPa
Fatigue limit in pure alternated tension σ_D	776 MPa
Steel grade	C92D (standard ISO 16120-2)

2.2. Plain fretting test: friction and wear analyses

To investigate the surface wear phenomenon, plain fretting tests were performed using a single actuator MTS hydraulic rig, which is displayed in Figure 1. The loading wire is in contact with the specimen wire at an angle $\beta = 30°$, and a constant normal force P is applied with a spring-screw system connected to normal force arms. The specimen wire is fixed. An actuator applies a cyclic sinusoidal displacement $\delta(t) = \delta^* \cdot \sin(2\pi ft)$. A load cell measures the tangential force Q(t). Note that the measured displacement amplitude is rig-dependant, as it depends on the rig stiffness. The wires are cleaned with ethanol before being put in contact.

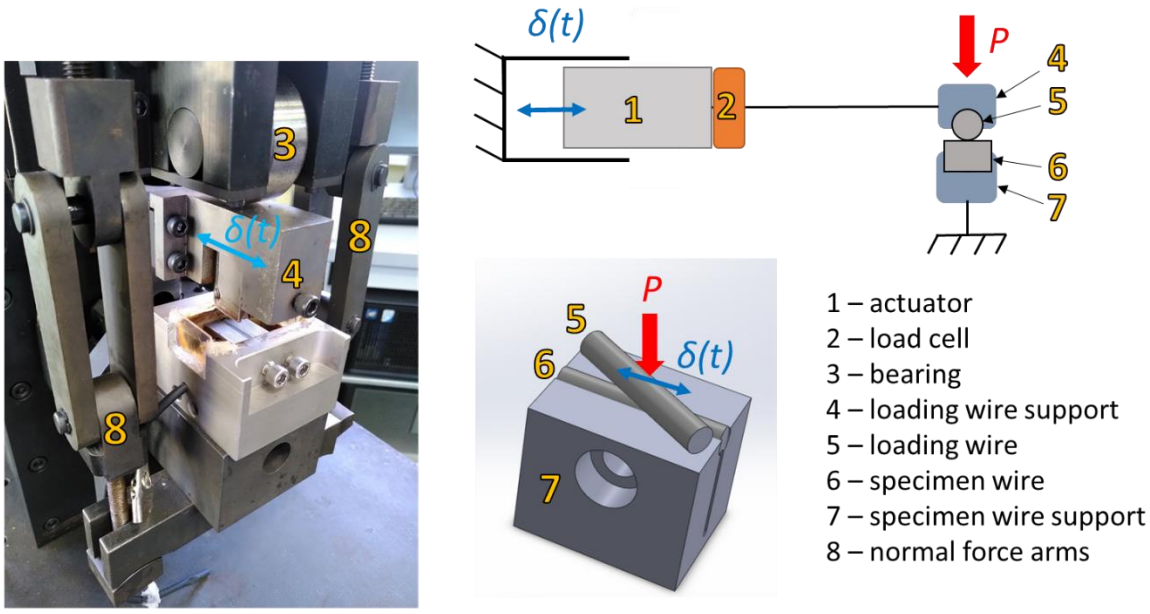

(a)

Figure 1: (a) plain fretting test rig.

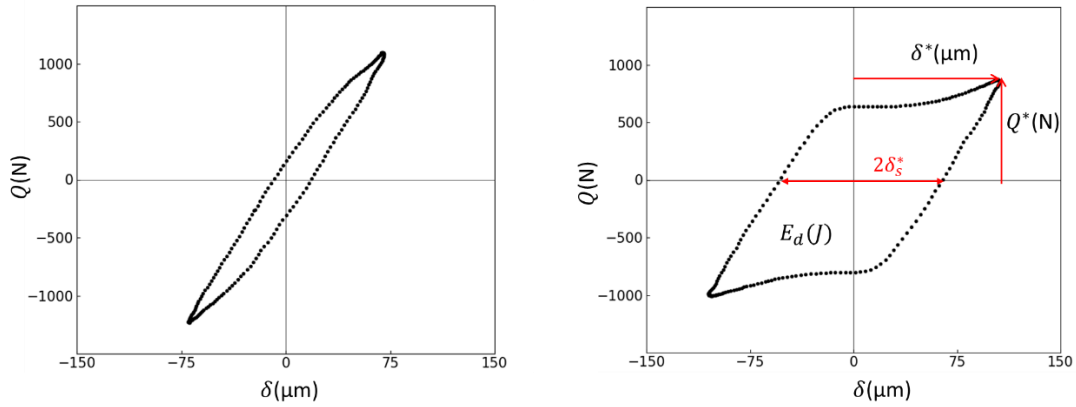

(a) (b)

Figure 2: fretting loops extracted from plain fretting ($P = 1400$ N) (a) partial slip, (b) gross slip

Figure 2 displays fretting loops in partial slip and gross slip. A very distinct evolution is observed. Partial slip displays a closed fretting loop whereas gross slip is characterized by an open hysteresis. The tangential force amplitude Q^*, the displacement amplitude δ^* and the friction energy related to the area of the hysteresis are extracted from these fretting loops. The sliding amplitude δ_s^* is estimated by measuring the residual displacement when the tangential force is zero: $\delta_s^* \simeq \delta^*(Q = 0)$ [18]. It is negligible under partial slip but significant under gross slip and will be considered to compute Archard's wear parameter. Note that the sliding

amplitude is not equal to the displacement value due to the contact and test system accommodations. If the fretting loop analysis is not possible, the sliding amplitude δ_s^* under gross slip can also be estimated from δ^* such that:

$$\delta_s^* = \delta^* - \delta_t^* \cdot \frac{\mu_{GS}}{\mu_t} \quad (1)$$

Figure 3 displays the tangential force amplitude Q^* as a function of the displacement amplitude δ^*. Increasing δ^* leads first to a quasi linear rising of Q^* until it reaches a maximum value $Q_t^* = \mu_t \cdot P$ at the partial slip/gross slip transition, with $\mu_t \simeq 0.9$. When the contact shifts to gross slip, Q^* drops, as the friction coefficient in gross slip is $\mu_{GS} \simeq 0.7$.

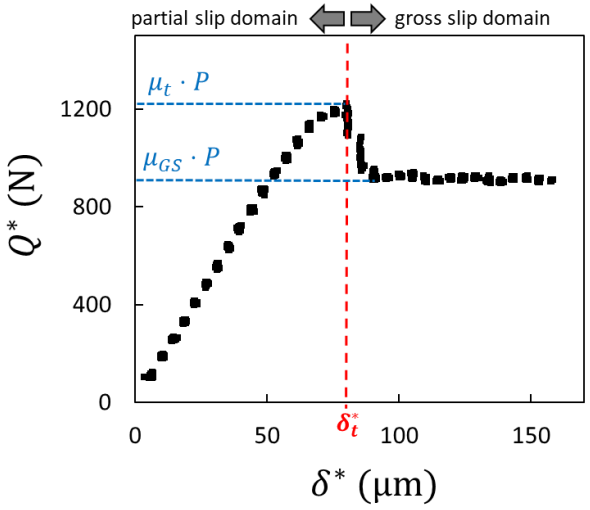

Figure 3: Evolution of Q^*as a function of δ^* using a variable displacement test method on plain fretting test rig ($P = 1400$ N).

2.3. Fretting fatigue test rig

The fretting fatigue tests were conducted on a two-actuator MTS hydraulic rig, displayed in Figure 4. Like for plain fretting test, wires were contacted with an angle $\beta = 30°$. A polymer pad is placed on the opposite side to prevent specimen bending. Its material and shape were chosen to minimise friction. A constant normal force is applied using a sliding rail and a spring-screw system allowing the application of a constant normal force. The fretting actuator displacement $\delta_{FA}(t) = \delta_{FA}^* \cdot \sin(2\pi ft)$ induces a displacement of the loading wire. Load cells measure forces $F_A(t)$ and $F_B(t)$ on both extremities of the specimen. The total tangential force $Q_{tot}(t)$ involving the crossed wires contact plus the polymer contact is given by:

$$Q_{tot}(t) = F_B(t) - F_A(t) \quad (2)$$

The amplitude of the tangential force related to the single crossed wires contact is deduced by:

$$Q^* = Q^*_{tot} - Q^*_{pp} \quad (3)$$

where Q^*_{pp} is the amplitude of the tangential force applied by the polymer pad, which was identified doing a test with two polymer pads for equivalent contact conditions.

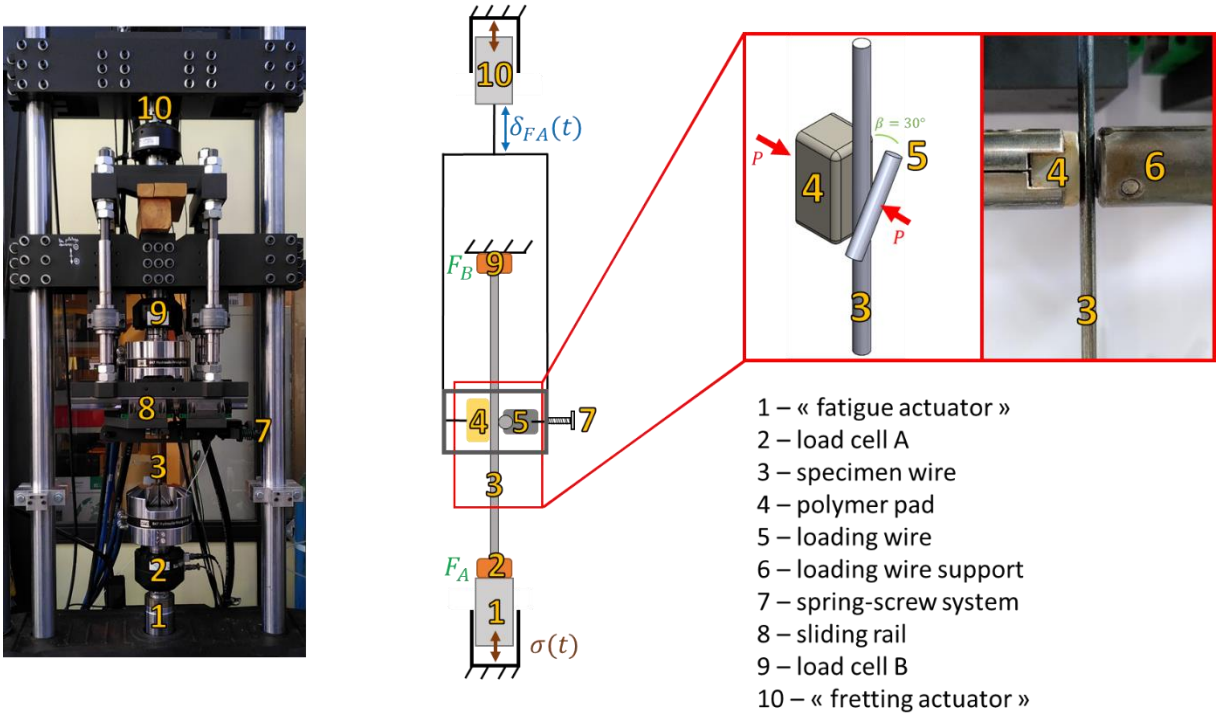

Figure 4: fretting fatigue test rig

The "fatigue actuator" applies a cyclic force $F_A(t)$ to the specimen. The use of two actuators allows to decouple fretting and fatigue loadings. The actuators move in phase, at the same frequency f. The setpoint of the fatigue actuator is automatically adapted so that F^*_B stays constant even with changing Q^*_{tot}. The fatigue load is therefore given by:

$$\sigma = \sigma_m + \sigma_a \cdot \sin(2\pi ft) = \frac{F_B}{S} \quad (4)$$

where S is the specimen cross-section area.

Figure 5 displays the evolution of tangential force amplitude Q^*_{tot} as a function of fretting actuator displacement amplitude δ^*_{FA}, obtained with a variable displacement test with constant fatigue amplitude. In-phase displacement of the actuators leads to this typical non-monotonic $Q^*_{tot}(\delta^*_{FA})$ curve. When the fretting actuator is not moving (i.e., $\delta^*_{FA} = 0$), a fretting load is generated by the elongation of the specimen due to the fatigue actuator load. Increasing δ^*_{FA}, the relative mismatch between the fatigue elongation of the specimen and the fretting displacement decreases, so Q^*_{tot} decreases, until the fatigue elongation is fully compensated at $\delta^*_{FA} = \delta^*_{FA,0}$. Further increase of δ^*_{FA} promotes a reverse mismatch, leading to an increase of Q^*_{tot}, until it reaches a maximum at the partial slip/gross slip transition.

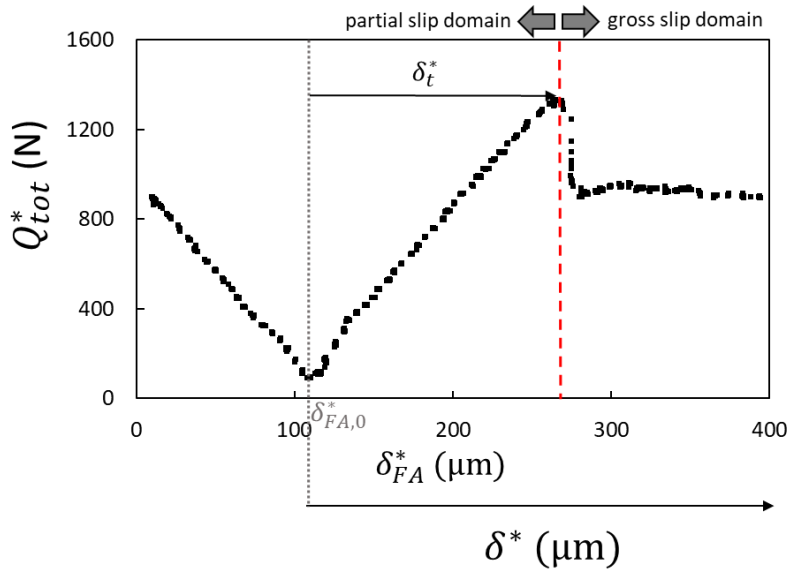

Figure 5: variable displacement test on the fretting fatigue test rig with constant fatigue amplitude. $P = 1400$ N, $\sigma_m = 320$ MPa, $\sigma_a = 160$ MPa

For better readability of the figures, instead of using the displacement amplitude of the fretting actuator δ^*_{FA}, we will consider an effective displacement amplitude δ^* defined as:

$$\delta^* = \delta^*_{FA} - \delta^*_{FA,0} \quad (5)$$

For the tests, we chose to exclusively use the $\delta^*_{FA} \geq \delta^*_{FA,0}$ domain.

Hence, for each δ^*, we measure Q^*_{tot}, and applying equation (3), we can deduce the effective Q^* tangential force amplitude.

2.4. Contact configuration

Figure 6 illustrates the contact morphology induced by a $\beta(X1;X2) = 30°$ crossed wires configuration. An elliptical shape is observed with a major angle axis X following the median position between X1 and X2 so that $\gamma = \frac{\beta}{2} = 15°$. This elliptical contact is characterized by the semi-major contact radius a_X along X and the semi-minor contact radius a_Y along the perpendicular direction Y. Under partial slip condition, an elliptical inner stick zone is operating leading to the corresponding c_X and c_Y stick radius. Note that for the perpendicular crossed wires situation $\beta = 90°$, an equivalent sphere/plane contact situation is observed so that $a = a_X = a_Y$ and $c = c_X = c_Y$. Finally the contact area is simply estimated by :

$$A_w = \pi \times a_X \times a_Y \quad (6)$$

These various length scale variables (i.e. a_X, a_Y, c_X, c_Y, A) will be measured on the fretting scars or computed using the model.

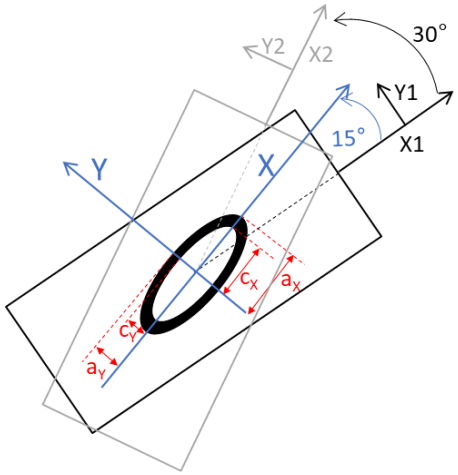

Figure 6 : Elliptical fretting scar (partial slip contact) related to the studied 30° crossed wires contact configuration.

3. Experimental results and discussion

3.1. Fretting fatigue tests

Three series of experiments have been performed. The range of applied loads was chosen to be representative of the loads in a wire rope, and were identified through the FEM simulation of a wire rope (not developped here). A first series (called A) consists in imposing a constant normal load $P = 1400\ N$ and a constant fatigue stress ($\sigma_m = 320\ MPa, \sigma_a = 160\ MPa$) but varying the contact displacement δ^* from partial slip to gross slip. These results will be more deeply investigated since our objective is to investigate and simulate the effect of wear on fretting fatigue. Two other series of experiments, called B and C, running under partial slip condition have been also performed to confirm the given fretting fatigue model. Series B consists in keeping the same fatigue loading as A but decreasing the normal load to $P = 500\ N$. The tangential forces were kept below the gross slip transition. Series C consists in maintaining a constant partial fretting loading $P = 1400\ N$ and $Q^* \simeq 1000\ N$, a constant fatigue mean stress $\sigma_m = 320\ MPa$ but varying the fatigue stress amplitude from $\sigma_a = 36\ MPa$ to $\sigma_a = 160\ MPa$. All these experiments have been performed at a constant $f = 10\ Hz$ frequency under ambiant room temperature.

Table 2 : Compilation of the experimental results and related loading stress (i. e σ_{SWT,ℓ_d} , paragraphs 4.1.4 and 4.1.5).

Table 2 : compilation of the test conditions in fretting fatigue endurance

Series	P (N)	δ^* (µm)	Q^* (N)	SC	σ_m (MPa)	σ_a (MPa)	N_f	σ_{SWT,ℓ_d} (MPa)

A	1400	9	88	PS	320	160	$> 10^6$	615
A	1400	17	141	PS	320	160	$> 10^6$	776
A	1400	19	147	PS	320	160	500 000	787
A	1400	27	273	PS	320	160	370 000	1101
A	1400	48	460	PS	320	160	167 000	1331
A	1400	81	673	PS	320	160	121 000	1405
A	1400	106	860	PS	320	160	107 000	1339
A	1400	145	1090	PS	320	160	74 000	1350
A	1400	165	1152	GS	320	160	$> 10^6$	XX
A	1400	210	1264	GS	320	160	$> 10^6$	XX
A	1400	260	1330	GS	320	160	$> 10^6$	XX
B	500	19	203	PS	320	160	236 000	874
B	500	33	290	PS	320	160	311 000	959
C	1400	140	1004	PS	320	100	223 000	1321
C	1400	140	953	PS	320	49	610 000	1284
C	1400	140	1008	PS	320	36	1 190 000	1265

Figure 7.a displays the lifetimes of series A in fretting fatigue as a function of the displacement amplitude δ^*. A log scale was used for the lifetime axis. Figure 7.b displays the corresponding normalized tangential force amplitudes averaged over the whole duration of the tests, noted Q^*/P. The dotted vertical line at $\delta^* = 150$ µm represents the partial slip/gross slip transition.

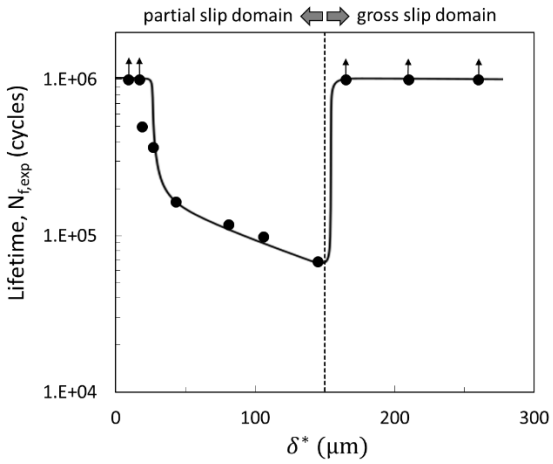

(a)

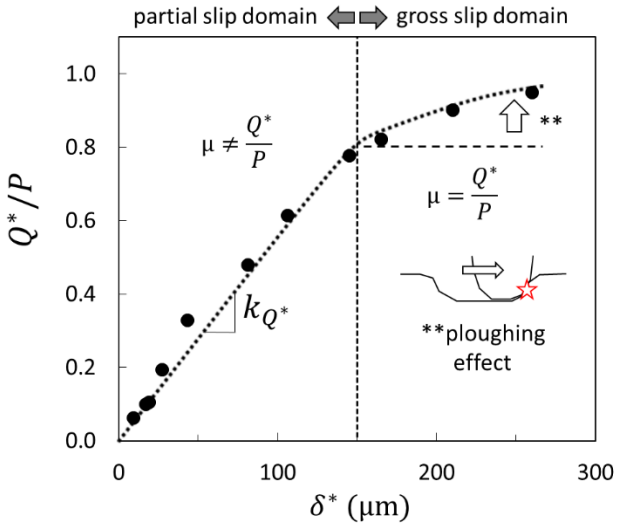

(b)

Figure 7: (a) evolution of the fretting fatigue lifetimes as a function of the effective displacement amplitude; (b) normalized tangential force amplitudes averaged over the duration of the test as a function of the effective displacement amplitude. Fretting fatigue tests with same fatigue loads and normal forces ($\sigma_m = 320$ MPa, $\sigma_a = 160$ MPa, $P = 1400$ N)

Below $\delta^* = 20$ µm, the fretting loads are too small to induce crack initiation, so the lifetime is above 10^6 cycles. A crack initiation threshold is observed at $\delta^* = 20$ µm above which the endurance sharply decreases. Between $\delta^* = 40$ µm and $\delta^* = 150$ µm, the endurance decreases as the tangential force increases since cracks initiate faster. Above $\delta^* = 150$ µm, the contact is

running under gross slip regime, and the lifetime rises up above 10^6 cycles. This can be related to the surface wear, which have two beneficial effects: "rubbing out" the cracks before they can propagate; and extending the contact area, thus reducing the cyclic shear and pressure stresses. The "U" shape of the lifetime curve was abundantly investigated in the literature [13, 19, 20]. The lowest endurance is systematically observed at the partial slip/gross slip transition, followed by an increase in the lifetime when gross slip and surface wear operate. In our case, this increase is very sharp. It is interesting to note that the Q^*/P ratio is still rising under gross slip domain. Fouvry et al. [21] observed a similar tendency on Ti-6Al-4V, which was explained assuming a ploughing effect, at the scale of the overall contact. Wear creates a depression in the specimen, promoting a tangential force peak at each border of the fretting cycle. This effect is better illustrated in Figure 8 where two fretting loops are compared after 20 000 and 100 000 fretting cycles respectively. After 20 000 fretting cycle, the depression is not formed and a rather flat evolution of the tangential force Q is observed during the sliding plateau. Beside the tangential force amplitude at the onset sliding sequence Q_{fs} remains unchanged whatever the test duration since at this instant of the fretting cycle, the counterface did not yet interact with the depression border.

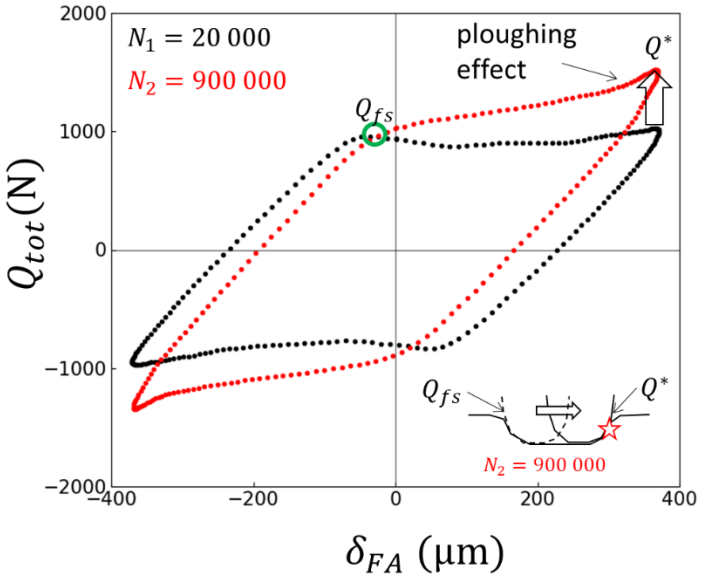

Figure 8: Illustration of the fretting loops evolution and related ploughing effect under gross slip condition (fretting fatigue test at $\delta^* = 260$ µm)

3.2. Fretting wear analysis

Figure 9.a displays the evolution of contact area at the end of the fretting fatigue tests as a function of displacement amplitude. A zoom on the partial slip domain is included. Figure 9.b,c shows pictures of the fretting scars at the end of the tests in the partial and gross slip domains. In the gross slip domain, the contact area increases significantly with the displacement amplitude, which was expected since gross slip wear is activated. The partial slip fretting scar is more interesting. The contact area also increases with the displacement amplitude. This is unexpected since according to the Mindlin's theory, the contact area should remain constant [22]. For very small δ^* close to zero, the contact area is close to the analytical prediction, given by Johnson's formalism [23]. However, the contact extension under large δ^* partial slip conditions needs to be explained.

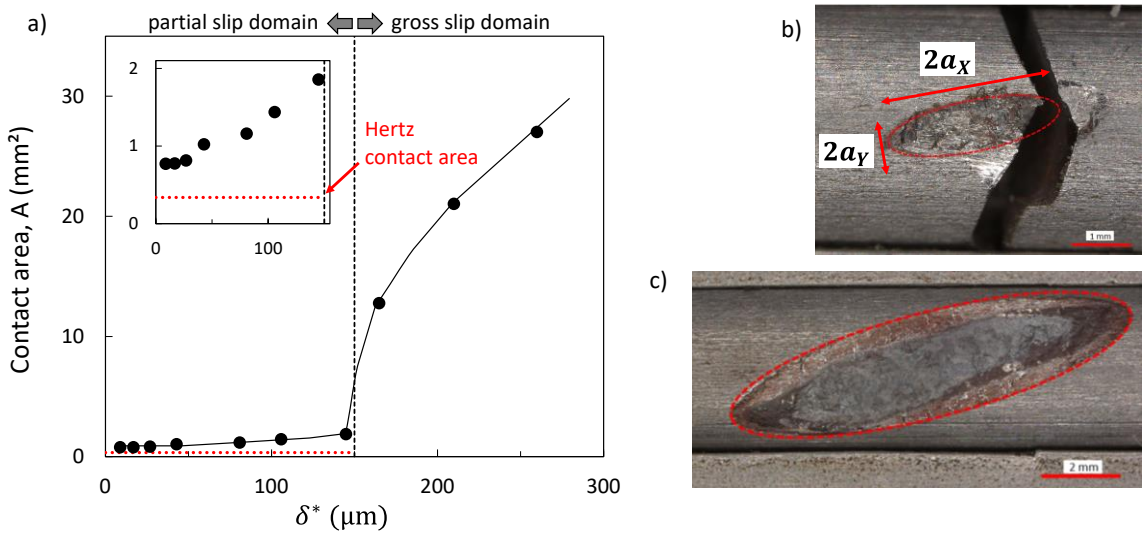

Figure 9: a) Evolution of the contact area at the end of the fretting fatigue tests as a function of the displacement amplitude, b) fretting scar for a test at $\delta^* = 145$ µm (partial slip), c) fretting scar for a test at $\delta^* = 210$ µm (gross slip)

Fretting fatigue tests with specimen failure is not appropriate to investigate the fretting wear contact extension, as the failure induces severe fretting scar deformations. To avoid this limitation, and also better control the sliding conditions, additional plain fretting tests have been performed varying the displacement from partial to gross slip domains for a constant 10 000 fretting cycles duration. Figure 10 compares the fretting scars obtained. Note that the displacement amplitude is rig-dependant, so the comparison with Figure 9 is not direct. The 2D surface profiles of partial slip condition shows very narrow surface modifications. Therefore, to quantify the surface damages under partial slip condition, the contact area measurement from optical observations will be preferred to the conventional 3D surface wear volume analysis.

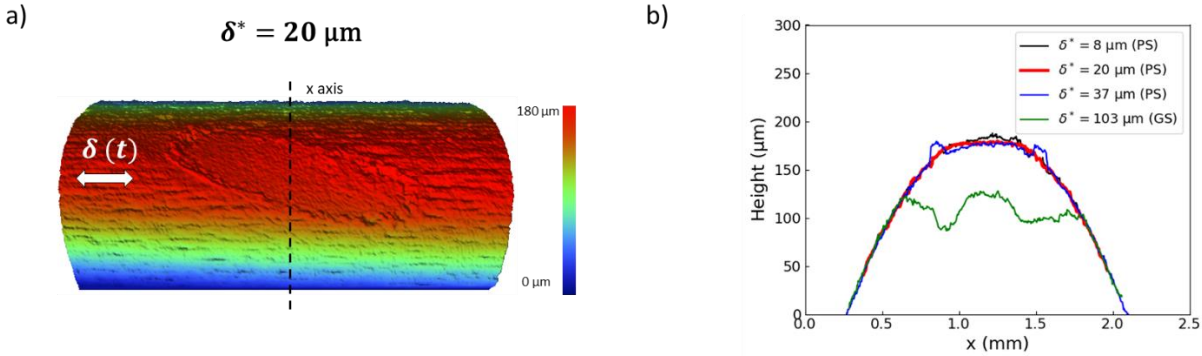

Figure 10: a) 3D wear profile of a fretting scar from a plain fretting test (10 000 cycles, $\delta^* = 20$ µm), b) 2D wear profiles of plain fretting tests (10 000 cycles)

3.2.1. Fretting scar morphology under partial slip conditions

Figure 11a displays the corresponding fretting log obtained from a plain fretting test imposing a $\delta^* = 60$ µm plain fretting displacement amplitude. At the beginning of the test, gross slip is prevailing, before stabilizing in partial slip condition. As detailed by Zhou et al [24], the contact is in fact running under mixed fretting regime with a gross slip period at the beginning followed by a steady state partial slip condition when the friction coefficient rises up. However, for simplicity, we will talk about "partial slip conditions", which in fact correspond to a mixed fretting regime including a very short gross slip period followed by a very long partial slip response.

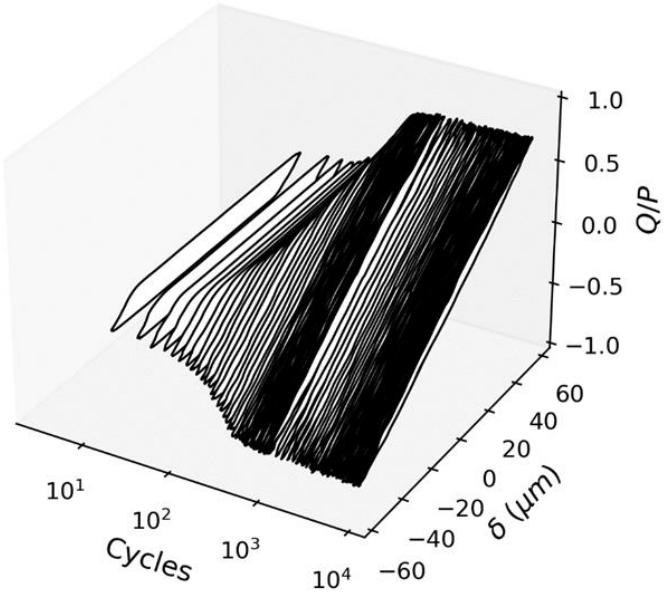

(a)

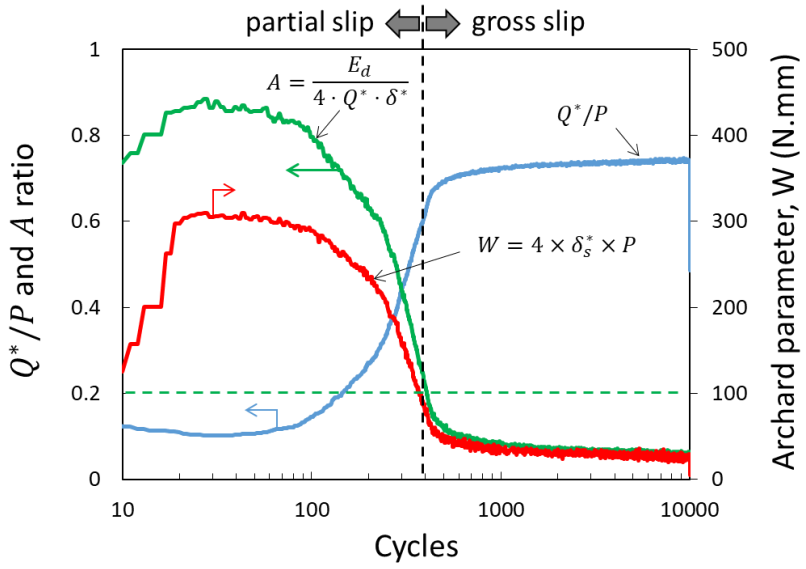

(b)

Figure 11: (a) fretting log of a plain fretting test at $\delta^* = 60$ µm, $P = 1400$ N (b) corresponding evolution of the Q^*/P ratio, energy sliding ratio A, and Archard work W dissipated per fretting cycle.

This mixed fretting sliding response is confirmed in Figure 11b where the corresponding Q^*/P and energy sliding ratio A evolutions are compared. The energy sliding ratio A expressed as [25] :

$$A = \frac{E_d}{E_t} = \frac{E_d}{4 \cdot Q^* \cdot \delta^*} \quad (7)$$

with E_t the total energy of the fretting cycle, allows to quantify if a fretting cycle is running under partial slip (i.e. energy sliding ratio is lower than 0.2) or under gross slip condition (i.e. energy sliding ratio is higher than 0.2). It clearly indicates that below N=500 cycles, the contact is running under gross slip. However with the rising of the coefficient of friction, the A ratio value decreases and after 500 cycles for the given displacement amplitude, the operating friction coefficient becomes high enough to shift the contact toward a partial slip contact response involving the formation of an inner stick zone. Q^*/P ratio then stabilise at constant value. Note that under partial slip, the Q^*/P ratio is no more equal to the friction coefficient as a significant part of the tangential force is in fact related to the elastic accommodation of the inner stick zone [26]. To complete the analysis the corresponding Archard factor parameter dissipated per fretting cycle W is plotted [27]:

$$W = 4 \times \delta_s^* \times P \quad (8)$$

The Archard factor parameter is significant during the transient gross slip period, indicating that surface wear is occurring at the beginning of the test. It decreases to zero when the partial slip condition stabilizes, suggesting that no additional surface wear degradation is occurring. This tendency is confirmed in Figure 12 where interrupted tests allows the plotting of the measured contact area as a function of the applied fretting cycles. The contact area increases from the initial unworn Hertzian estimation until the contact shifts to the partial slip condition. It is surprising to note that despite the very short period of the gross slip sequence, the contact area extension is significant (i.e. above a factor 5 for this $\delta^* = 60$ µm plain fretting test condition).

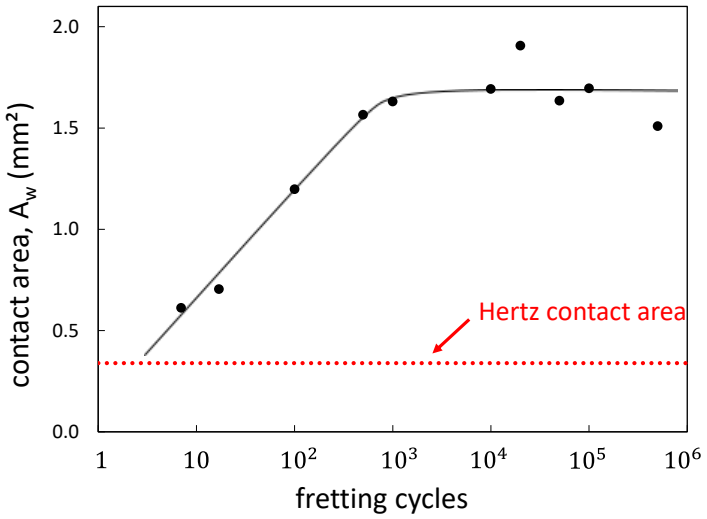

Figure 12: contact area evolution as a function of the number of cycles (interrupted plain fretting tests) ($P = 1400$ N, $\delta^* = 60$ µm).

This investigation confirms that the surface wear observed under partial slip domain is in fact induced by the transient gross slip period during which the coefficient of friction rises until

satisfying the partial slip condition. When the partial slip condition is stabilised, there is no more additional extension of the contact area.

This investigation was extended for different plain fretting displacement amplitudes, keeping constant the test duration at 10 000 fretting cycles. The displacement amplitude is rig dependent, therefore the wear analysis was done comparing the measured a_X and a_Y fretting scar radius as a function of the mean tangential force amplitude Q^* (Figure 13). Linear rising evolution are observed suggesting that the longer the displacement amplitude, the higher Q^*, the longer the transient gross slip period, the larger the Archard work dissipated during this period and finally the larger the contact area extension. Fretting fatigue results are also included in the analysis. The very good correlation with plain fretting data confirms the Q^* tangential force amplitude is a pertinent parameter to quantify the contact area extension under partial slip condition. It also confirms that plain fretting tests are representative of wear phenomena generated under fretting fatigue conditions. Currently, research works are undertaken to explain the linear relationships between the contact radius and the steady state partial slip tangential force amplitude. They require complex couplings between the evolution of the coefficient during the transient gross slip period and the evolution of the fretting loop shape. In the frame of this investigation focused on the fretting fatigue cracking process, we will restrict our analysis by considering simple linear functions so that:

$$\begin{aligned} a_X &= k_{a_X} \times Q^* + a_{X0} \\ a_Y &= k_{a_Y} \times Q^* + a_{Y0} \end{aligned} \qquad (9)$$

with $k_{a_X} = 5.4 \cdot 10^{-4}$ mm/N and $k_{a_Y} = 2.8 \cdot 10^{-4}$ mm/N the linear coefficients of the worn contact radius extension related to X and Y axis respectively (i.e. extracted from the experimental data) and a_{X0} and a_{Y0} the corresponding contact radius without gross slip wear period which can be approximated using the Hertz approximation so that for $P = 1400$ N, $a_{X0} = 0.77$ mm and $a_{Y0} = 0.14$ mm.

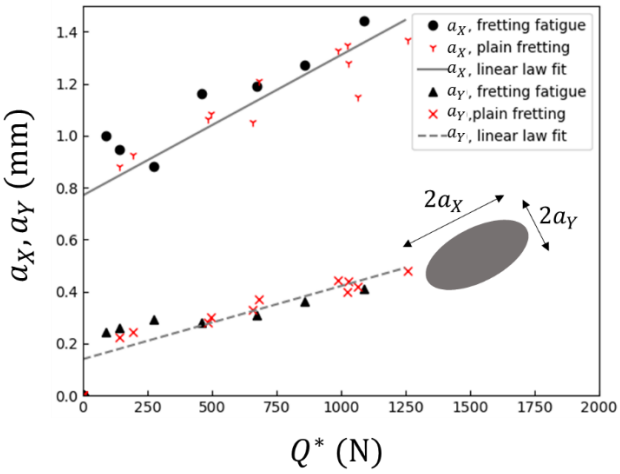

Figure 13: Evolution of the measured contact radius a_X and a_Y related to partial slip domain as a function of the corresponding mean tangential force amplitude Q^*. This analysis includes plain fretting tests interrupted after 10^4 cycles and fretting fatigue tests expertised at the end of the test ($P = 1400$ N).

A crucial aspect is the pressure profile evolution that can be extrapolated from these contact radius fluctuations. When the surface wear is severe, flat contact pressure profiles are usually adopted. However, Figure 10 suggests rather small wear volumes for these partial slip conditions. Hence an elliptical pressure profile approximation will be assumed in a first approach replacing in Hertzian formalism the updated contact radius a_X and a_Y derived from Eq. (9). An indirect approach to justify this hypothesis consists in comparing the evolution of the corresponding stick radius c_X and c_X. Indeed, assuming a non-conformal contact, and Hertzian hypotheses, Cattaneo [28] demonstrate that the ratio between the semi-axes of the stick zone ellipse and the contact ellipse, is given

$$\left(\frac{c_X}{a_X}\right)^3 = \left(\frac{c_Y}{a_Y}\right)^3 = \left(1 - \frac{Q^*}{\mu P}\right) \qquad (10)$$

where μ is the local friction coefficient in the sliding zone which can be approximated by the friction coefficient measured at the sliding transition μ_t [29].

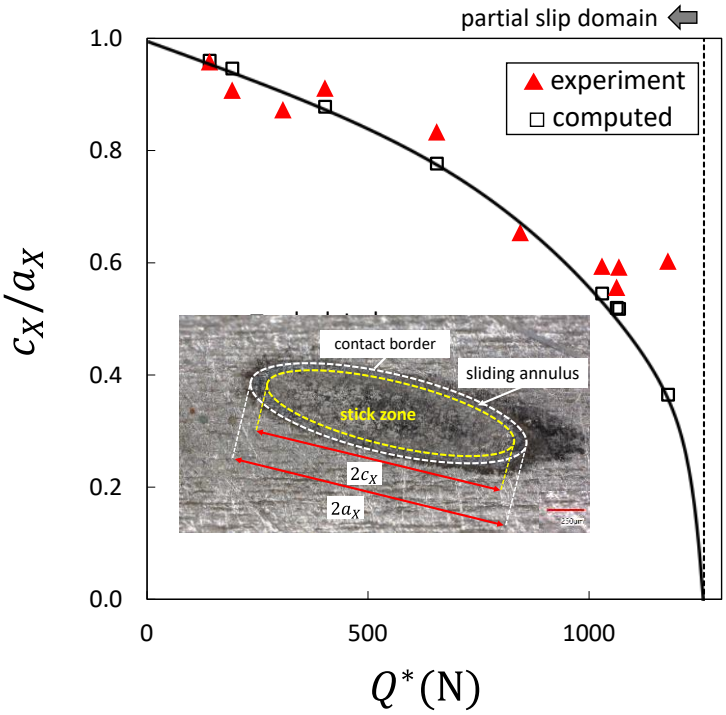

Figure 14: Evolution of c_X/a_X measured from fretting scar expertise (plain fretting tests after 10 000 cycles), and Cattaneo's [28] theoretical prediction.

A very nice correlation is observed suggesting that the theoretical formalism well depicts the experiments. A larger discrepancy is however observed for the highest tangential forces conditions. The experimental ratio seems to be higher than the calculated one. This is coherent with the pressure and shear profiles flattening due to a larger surface wear generated during the transient gross slip period when the contact coating is next to the gross slip domain boundary. Besides for stabilized tangential force amplitudes higher than 1000 N, the frontier between stick and slip zones is less easily defined, so that confidence regarding c_X/a_X ratio is lower. To conclude it can be stated that Cattaneo's formalism predicts well the c_X/a_X contact morphology. This indirectly confirms the Hertzian approximation and therefore the elliptical pressure profile hypothesis.

3.2.2. Fretting scar morphology under gross slip conditions

As illustrated previously in Figure 10, surface wear under gross slip is significant justifying to quantify the contact area evolution as a function of the wear volume extension. Figure 15 plots the evolution of the wear volume obtained from various gross slip plain fretting and fretting fatigue condition as a function of the corresponding accumulated Archard parameter :

$$\sum W = 4 \cdot P \cdot \delta_s^* \cdot N_c \quad (11)$$

where N_c is the number of loading cycles applied.

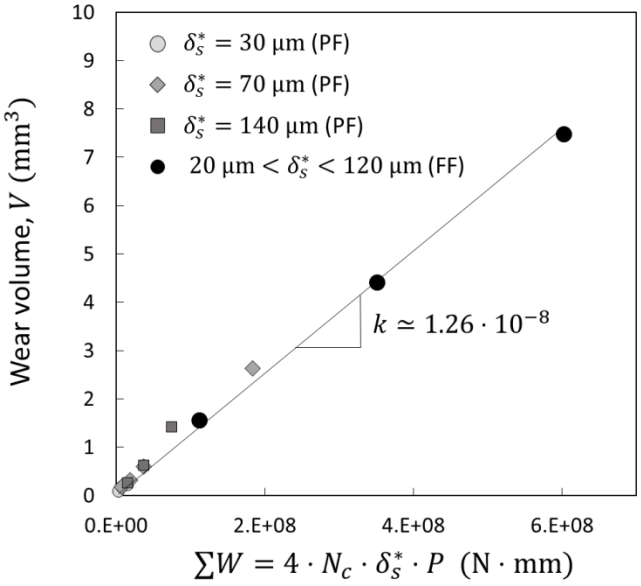

Figure 15: wear volume as a function of the accumulated Archard parameter $(\sum W)$ plain fretting and fretting fatigue tests ($P = 1400$ N; $N_c \in \{20\,000,\ 50\,000, 100\,000\}$; $\delta_s^* \in \{30\ \mu m, 70\ \mu m, 140\ \mu m\}$.

A linear evolution is observed suggesting that the wear volume V extension can be approximated using the Archard theory:

$$V = k_w \cdot \sum W \quad (12)$$

with $k_w \simeq 1.2 \cdot 10^{-8}$mm^3/(N·mm) being the so called Archard wear coefficient. Various formulations have established to extrapolate the contact area extension of simple Hertzian contact configurations as a function of the wear volume. For instance, based on geometrical considerations, the sphere/plane contact area extension can be expressed as a ½ power law function of the wear volume [30]:

$$A_w = A_H + k_A \times V^{1/2} \quad (13)$$

with A_H the Hertzian contact area and k_A a geometrical coefficient.

The contact radius extension is then deduced from the following simple relationship:

$$a_w = a_H + k_a \times V^{1/4} \quad (14)$$

with a_H the Hertzian contact radius and k_a a geometrical coefficient.

The contact configuration of the studied crossed cylinders configuration (i.e. $\beta < 90°$) is more complex to address. To our knowledge there are no explicit formulations linking the wear volume to the operating contact area for such kind of contact assembly. Hence a numerical strategy is considered. Let us consider two cylinders C_1 and C_2 of radius R, in contact, inclined at an angle β, as illustrated in Figure 16.a. If we decrease the distance between the cylinders so that they interpenetrate each other, the intersection volume corresponds to the wear volume of the two cylinders. The projection of this intersection volume on the plane perpendicular to the contact normal is the contact area. Obtaining an analytical expression of this relationship for $\beta = 30°$ is too complex, we thus decided to use a numerical approximation. Consider a three-dimensions grid (x, y, z) with step sizes $(\Delta x, \Delta y, \Delta z)$. We evaluate each node: inside/outside C_1, inside/outside C_2. The wear volume is calculated as the number of nodes inside both C_1 and C_2, multiplied by the nodal volume $\Delta v = \Delta x \cdot \Delta y \cdot \Delta z$. The contact area is calculated similarly as the projection on the (O, x, z) plane of the nodes on the wear volume, multiplied by $\Delta x \cdot \Delta z$. Figure 16.b displays a 2D description of this process (the displayed step sizes are bigger for clarity).

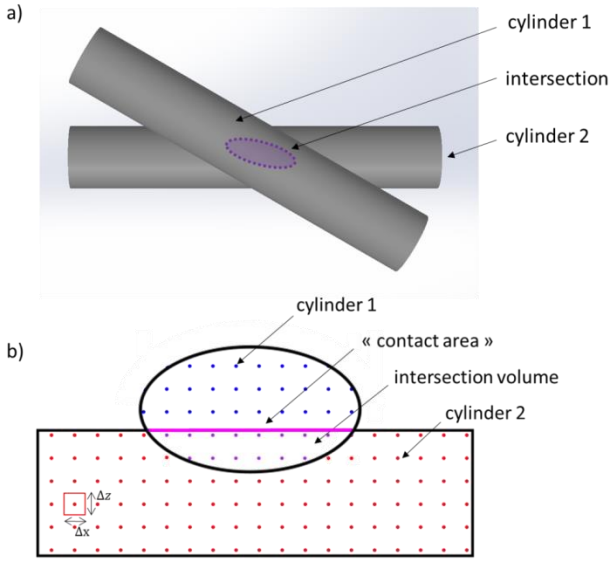

Figure 16: (a) interpenetration of two crossed cylinders, (b) Cross section Illustration of the numerical approximation method used to determine the relationship between wear volume and observed contact area

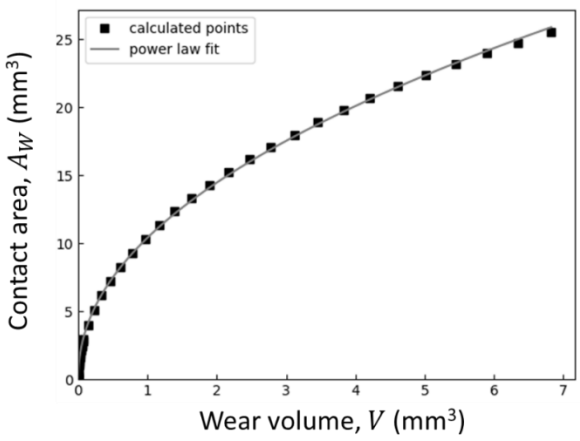

Figure 17: numerical approximation of the relationship between wear volume and contact area.

Figure 17 displays the evolution of contact area A_w as a function of the wear volume V derived from this numerical analysis. A power law was fitted on the calculated data points:

$$A_w = A_{w,\emptyset} \cdot V^{\beta_{A_w}} \quad (15)$$

with $A_{w,\emptyset} = 11.5$ and $\beta_{A_w} = 0.47$.

From this contact area analysis, both a_X and a_Y semi-axes parameters can be extrapolated. The contact major semi-axis $2a_X$ is calculated as the maximum of the distances between all pairs of nodes in the wear volume, and $2a_Y$ is calculated with the following formula:

$$a_Y = \frac{\text{contact area}}{\pi \cdot a_X} \quad (16)$$

Again power laws can be considered determined to estimate both a_X, a_Y from the wear volume computation :

$$a_X \simeq a_{X0} \cdot V^{\beta_{a_X}}, \quad a_Y \simeq a_{Y0} \cdot V^{\beta_{a_Y}} \quad (17)$$

with $a_{X0} = 3.54$, $\beta_{a_X} = 0.248, a_{Y0} = 0.921$ and $\beta_{a_Y} = 0.243$.

Therefore by extrapolating the wear volume from the Archard relationships (12) and coupling equations (15) to (17), the worn contact area and related ellipse contact radius can be approximated under gross slip domain. Note that since solid rigid hypotheses have been considered, this approximation cannot detail the presence of a residual elastic “Hertzian” component like previously implemented in the sphere/plane analysis [30] (i.e. Eq. (13) and (14). However, for high wear volume conditions, like presently observed, this residual value can be neglected and the given power law formulations (i.e. Eq. (15) and (17)) are representative. Besides it is interesting to note that the exponents of these power law functions are very close to

the explicit values derived for the sphere/plane analysis since $\beta_{A_w} = 0.47$ is nearly equivalent to ½ and $\beta_{a_X} \approx \beta_{a_Y} \approx 0.24$ is comparable to ¼. This suggests a possible explicit correlation between wear volume and contact area parameter for crossed cylinder conditions where in fact the sphere/plan contact (i.e. $\beta = 90°$) is a specific case.

4. Numerical model

Our objective is to formalize the fretting fatigue crack nucleation risk under either partial or gross slip conditions, taking into account the surface wear extension. Usual FEM fretting analysis simulates wear through a continuous remeshing which is quite complex and above all time consuming. To palliate such limitations, we propose an alternative hybrid strategy where the pressure and shear contact fields are computed analytically. These fields are then imposed to a 3D FEM model of the wire. Hence , the contact area extension derived from the experiment's analysis can easily be transposed to the FEM fretting fatigue analysis.

Figure 18 displays the complete algorithm of this approach. First, the regime (partial slip or gross slip) is given as an input, as wear behaves differently in these two domains. If the regime is partial slip, the dimensions of the contact ellipse are calculated taking into account the surface wear induced by the transient gross slip period and transposed in the elliptical Hertzian pressure and related Mindlin's shear field approximations. These pressure and shear contact stress fields are then applied to a 3D FEM model and combined with the fatigue load. A post-processing computes the Smith-Watson-Topper (SWT) equivalent fatigue stress parameter at a critical distance below the surface hotspot to capture the stress gradient effect. This value is then compared to the threshold fatigue limit value to evaluate if a crack will initiate or not. If the regime is gross slip, the algorithm is similar, however an additional loop is included to simulate wear using the Archard's law (equations (12) - (17)). A cumulative damage is computed to evaluate if the specimen will fail or not.

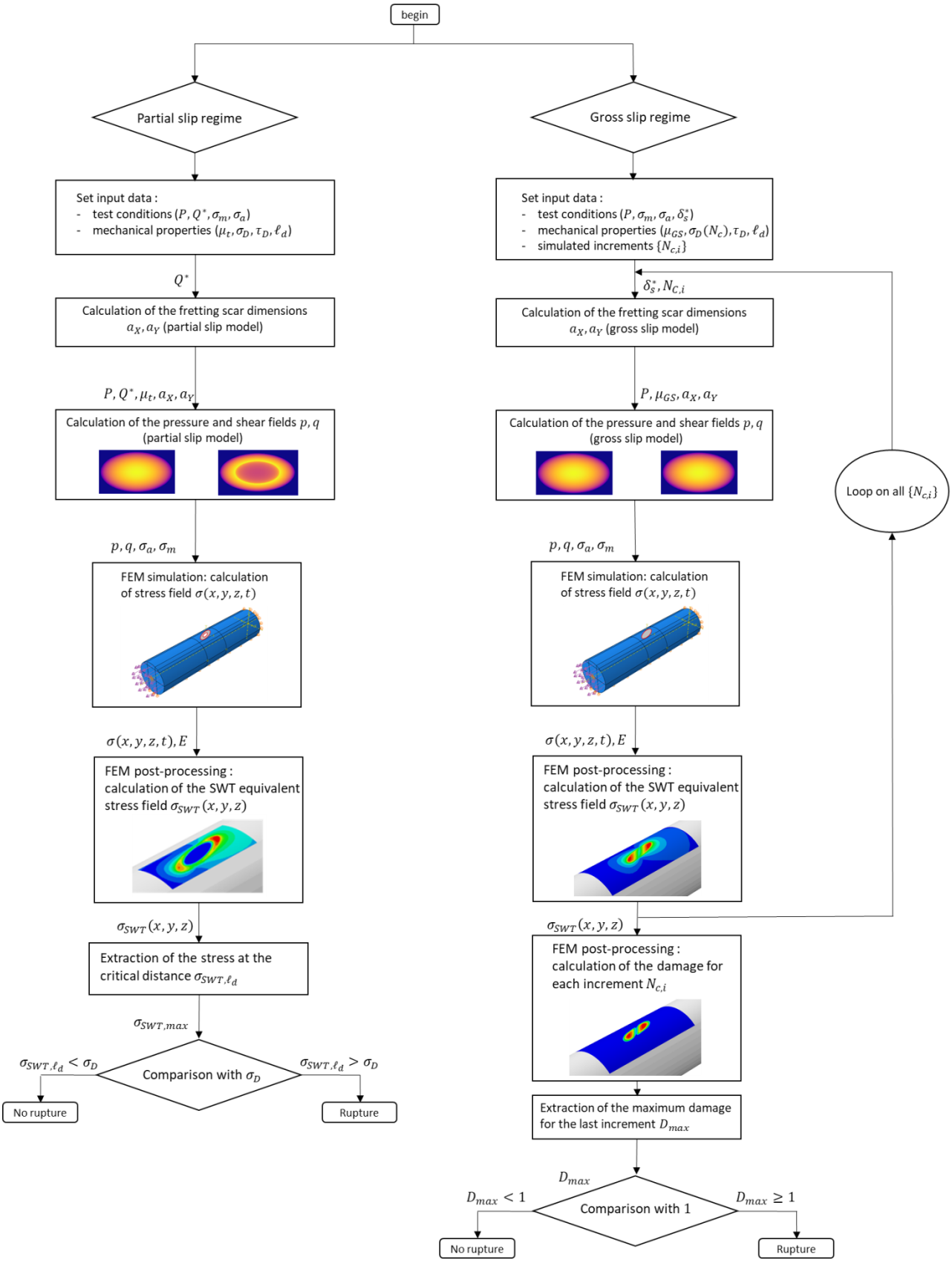

Figure 18: algorithm for crack initiation prediction

4.1. Partial slip domain algorithm

4.1.1. Fretting scar dimensions in the partial slip domain

If the regime is partial slip, then fretting scar dimensions are calculated using the input tangential force amplitude using the empirical relationship equation (9). The transient gross slip wear period is very short, so that it is considered as instantaneous. There is no need to simulate continous wear process.

4.1.2. Pressure and shear stress fields calculation

The contacting zone in a crossed-cylinders contact configuration (non-conformal contact) is an ellipse. A 2D coordinate system can be defined with the contacting point O as the origin, and Ox and Oy as the axes, with Oxy being the plane whose normal corresponds to the contacting normal and Ox, Oy in the directions of respectively the semi-major and semi-minor axes of the ellipse. Johnson [23] explains that the pressure field in the contacting zone is given by:

$$p(x,y) = p_0 \sqrt{1 - \left(\frac{x}{a_X}\right)^2 - \left(\frac{y}{a_Y}\right)^2} \quad (18)$$

where a_X, a_Y are the semiaxes of the contact ellipse, and p_0 is:

$$p_0 = \frac{3P}{2\pi a_X a_Y} \quad (19)$$

The partial slip shear stress profile is derived for Cattaneo [26] and Deresiewicz [29] formalism:

$$q(x,y) = \mu \cdot p_0 \sqrt{1 - \left(\frac{x}{a_X}\right)^2 - \left(\frac{y}{a_Y}\right)^2} \quad (20)$$

in the stick zone:

$$q(x,y) = \mu \cdot p_0 \sqrt{1 - \left(\frac{x}{a_X}\right)^2 - \left(\frac{y}{a_Y}\right)^2} - \left(1 - \frac{Q}{\mu P}\right)^{1/3} \cdot \mu \cdot p_0 \sqrt{1 - \left(\frac{x}{c_X}\right)^2 - \left(\frac{y}{c_Y}\right)^2} \quad (21)$$

where c_X, c_Y are the semiaxes of the no-slip ellipse, which can be calculated with:

$$\left(\frac{c_X}{a_X}\right)^3 = \left(\frac{c_Y}{a_Y}\right)^3 = \left(1 - \frac{Q}{\mu P}\right) \quad (22)$$

The coefficient of friction μ operating in the sliding zone can be approximated by the value measured at the partial slip transition (μ_t) [*29*].

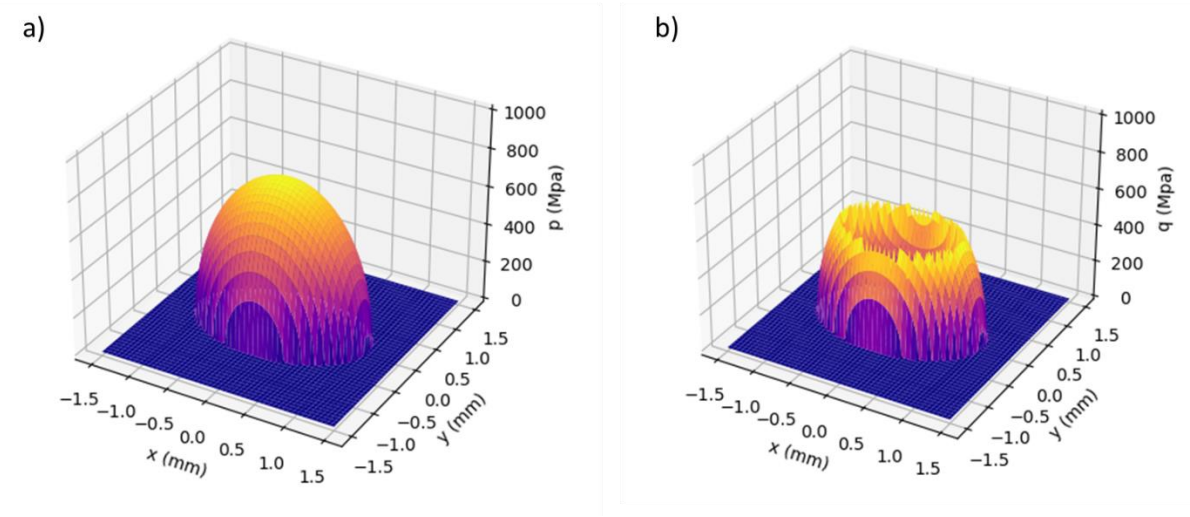

Figure 19: analytical a) pressure and b) shear stress fields (for a non-conformal contact)

This method relies on several assumptions. First, these formulas are valid when the Hertz assumptions are satisfied: the contact must be non-conformal and the contact zone very small compared the relative radius of curvature. This is not exactly the case here, as wear tends to flatten the surfaces and significantly increase the contact zone size. However, the comparison of sliding and stick areas in fretting scars done in Figure 14 suggests that the given formalism provides a good approximation of both pressure and shear stress fields. The wear generated during the transient period is small so the non-conforming hypothesis is justified. Additionaly, the fatigue stress amplitude is small comparatively to the constant pressure so the stick zone offset detailed by Nowell et al. [30] can be neglected.

4.1.3. Finite elements model

Figure 20 illustrates the FEM model of a wire on which cyclic fatigue stress, pressure and shear stress fields are imposed. The material is fully elastic steel ($E = 210$ GPa, $\nu = 0.3$). Reduced integration linear brick elements (C3D8R) were used. Mesh close to the contact is made of approximatively 20 µm edge length cubes, and is scarcer in the rest of the solid. At the "fixed" face, the displacement along z axis is constrained, while displacements along x and y axes are not, to allow for radial contraction of the wire. At the "counterbody" face, displacement along y is constrained, to prevent bending effects on the wire. The pressure and shear fields are applied along respectively y and z directions. There is a 15° tilt between local x, y axes used in equations (18)(20) and global model x, y axes. Indeed, the 30° angle between the contacting wires will induce a a 15° tilt of the contact ellipse as illustrated in Figure 6. The fatigue load is applied as a surface traction. Its amplitude is adapted to compensate the contact tangential force effect and to be consistent with experimental loading conditions:

$$\sigma_{a,imposed} = \sigma_a - Q^*/S \qquad (23)$$

where S is the radial section of the wire. In the experimental apparatus, this adaptation is done automatically through a feedback loop.

Only the two extreme loading states of the fretting cycle are simulated: in the first one, $\sigma(t_1) = \sigma_m + \sigma_a$ and $q(t_1) = +q$; in the second one $\sigma(t_2) = \sigma_m - \sigma_a$ and $q(t_2) = -q$. The pressure field stays constant. Using these two loading states the fatigue stress analysis can be performed.

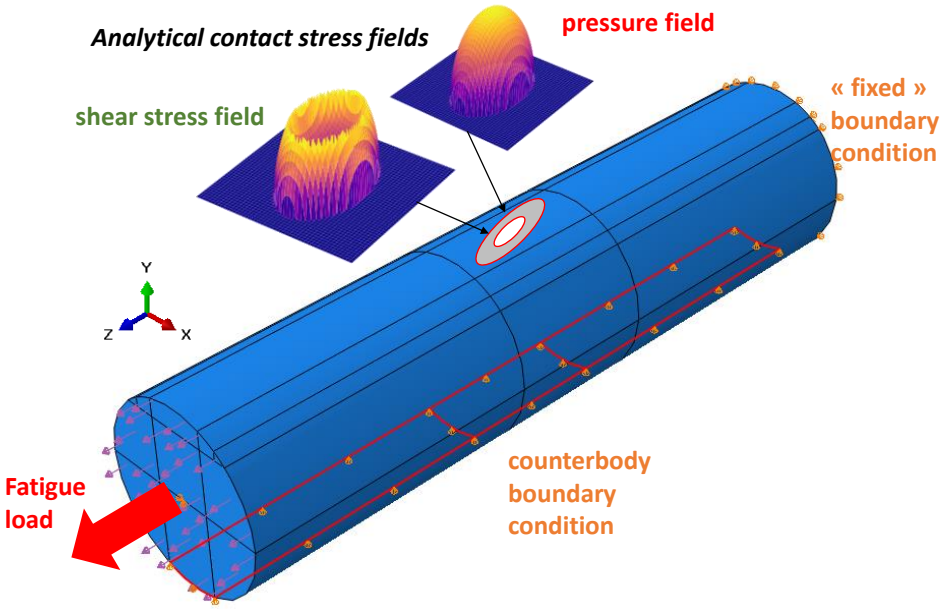

Figure 20: hybrid analytical-FEM modelling

Note that in the real contact, the geometry of the wire is modified by wear. The friction interface interface moves towards the inside of the wire. The model neglects this effect, and assumes that the wire maintains a perfect cylinder geometry. Only the pressure and shear fields are adjusted to take into account the wear contact area extension. This may induce a small error in the subsurface stress distributions. However this error is assumed negligible since the wear depth is about few tens microns whereas the extension of the contact area is of the order of a millimeter.

4.1.4. Multiaxial fatigue analysis

The Smith-Watson-Topper (SWT) multiaxial fatigue criterion [*33*] is applied to predict the cracking risk. This criterion is widely used for fretting fatigue (see [*34*, *35*, *36*]). SWT is

based on a critical plane approach, meaning that for each point in the solid, the parameter is calculated for every possible unit normal vector $\vec{n}$. For each point, for each $\vec{n}$ vector, σ_{max} is defined as the temporal maximum value of the normal stress:

$$\sigma_{max} = \max_{t \in T}(\|\bar{\bar{\sigma}}(t) \cdot \vec{n}\|) \quad (24)$$

For each point, for each $\vec{n}$ vector, ε_a is defined as the amplitude of deformation:

$$\varepsilon_a = \frac{1}{2} \cdot \max_{t_1, t_2 \in T}(\|\bar{\bar{\epsilon}}(t_1) \cdot \vec{n}\| - \|\bar{\bar{\epsilon}}(t_2) \cdot \vec{n}\|) \quad (25)$$

For each point, Γ_{SWT} parameter is defined as the maximum value of the product of σ_{max} and ε_a with varying $\vec{n}$:

$$\Gamma_{SWT} = \max_{\vec{n}}(\sigma_{max} \cdot \varepsilon_a) \quad (26)$$

An equivalent stress can be calculated as:

$$\sigma_{SWT} = \sqrt{E \cdot \Gamma_{SWT}} \quad (27)$$

This equivalent stress in then compared to the fatigue limit σ_d. If $\sigma_{SWT} < \sigma_d$, there is no crack nucleation. For $\sigma_{SWT} \geq \sigma_d$, a crack can nucleate. A Python post-processing script was applied to calculate σ_{SWT} at each integration point of the model. Figure 21.a shows the surface distribution of σ_{SWT} equivalent stress obtained from the simulation of the fretting fatigue test at $\delta^* = 145\ \mu m$ (corresponding to $Q^* = 1090\ N$). The black and white ellipses delimitate the slip and stick zones. As expected, the maximum value is located near the trailing edge, on the contact side were the fatigue stress is higher. This is consistent with the experimental observations: the cracks always appear on the upper bound of the fretting scar, as the stress amplitude on the upper part of the specimen is higher than on the lower part. This can be seen on Figure 21.b, which displays fretting scar for an interrupted fretting fatigue test, broken later with liquid nitrogen (this method allows to preserve the fretting scar, which is too damaged during rupture). Note that choosing to maintain F_B^* constant with changing Q_{sum}^* allows for a constant σ_a, which was our objective for establishing relevant $N_f - \delta^*$ fretting fatigue charts.

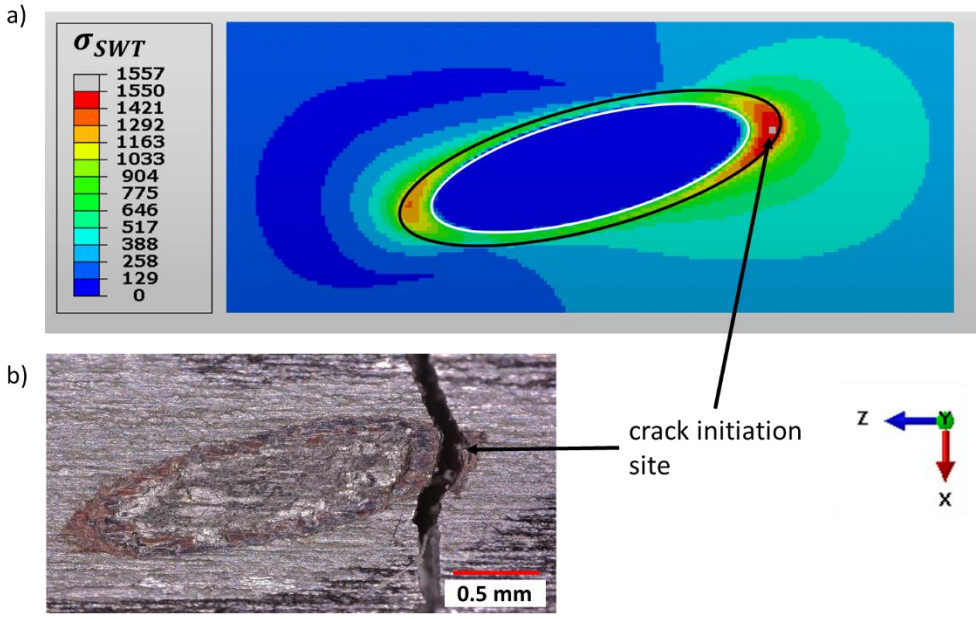

Figure 21: a) σ_{SWT} for the simulation of a fretting fatigue test at ($\sigma_m = 320$ MPa, $\sigma_a = 160$ MPa, $P = 1400$ N, $Q^* = 520$ N), b) fretting scar for the corresponding test, interrupted before failure and broken later with liquid nitrogen

4.1.5. Stress gradient effect correction

In fretting, the contact generates very localized high stresses. As a consequence, the failure criteria tend to overestimate the risk. This "stress gradient effect" was deeply investigated in the past decades using so-called "non-local" fatigue stress strategies like process volume averaging [34], line averaging, stress gradient correction [36] and critical distance method [37, 38]. A comparison between these various methods suggests that all of them lead to rather good results assuming that the corresponding length scale parameter used to capture the stress gradient effect is correctly estimated citation. For simplicity the critical distance method is presently adopted. It consists in considering the parameter not at the "hotspot", where it reaches its maximum value, but at a point located at a given distance under the hotspot. This distance seems to be load and material dependant, and much work has been done to link it to a physical parameter (see [38]), but no clear universal relationship has been found. In this paper, we simply identified it using the reverse approach proposed by Said et al [39], simulating the threshold cracking condition experimentally observed at $\delta^* = 17$ µm. Figure 22 plots the evolution of σ_{SWT} profile at the vertical of the hotspot. The values are calculated at the integration points of the elements, and is linearly interpolated between these points. As expected, σ_{SWT} at the hotspot is well over σ_d. The critical distance l_D is defined as the depth under the hotspot at which

$\sigma_{SWT} = \sigma_d$, and was found to be $l_D \simeq 25\ \mu m$. It is now possible to compute the failure criterion, and predict if a given fretting fatigue test will initiate cracks or not.

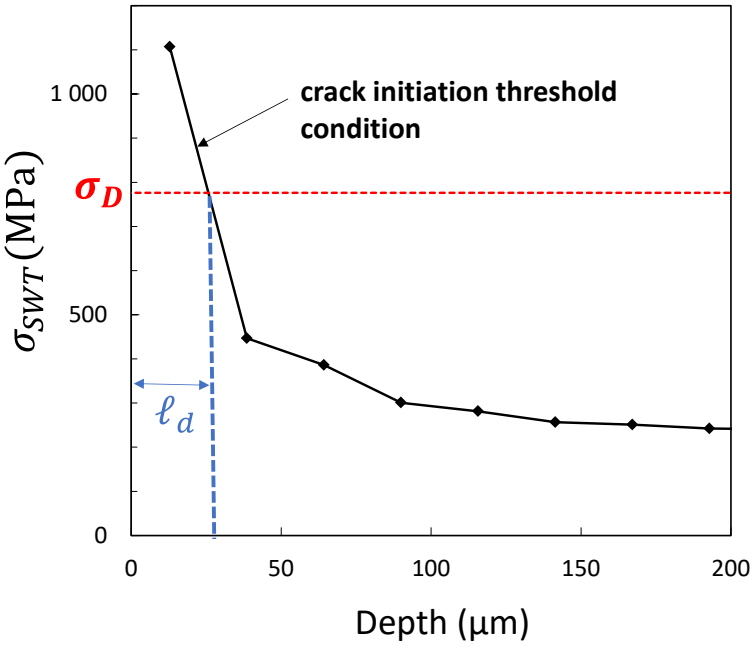

Figure 22: σ_{SWT} under the hotspot for the crack initiation threshold condition ($\sigma_m = 320$ MPa, $\sigma_a = 160$ MPa, $P = 1400$ N, $Q^* = 140$ N)

4.2. Gross slip domain algorithm

4.2.1. Fretting scar dimensions in the gross slip domain

Knowing the sliding amplitude δ_s^*, the normal force P and the number of cycles N_c, the model can estimate the wear volume and finally deliver the evolution of the fretting scar dimensions during the test.

4.2.2. Pressure and shear stress fields

In a first approximation, we still consider the non-conforming elliptical expressions to estimate the pressure profile p(x,y) (equation (18)) where a and b evolve with the wear extension. Finally, the cyclic shear profile under gross slip is given by:

$$q(x,y) = \mu_{GS} \cdot p(x,y) \qquad (28)$$

Former investigations [40] suggest that a flat pressure distribution is potentially more representative, however using elliptical approximations conservative stress fields are estimated.

4.2.3. Cumulative damage

Wear continuously modifies the fretting loads. To accelerate the computation, a jump cycle strategy used by McColl [12] and Cruzado et al [10] is implemented: the damage corresponding to ΔN_c cycles is simulated in a single numerical step. In classical wear modelling, increasing too much the increment ΔN_c leads to numerical instabilities. In our case this is not an issue, however, increasing ΔN_c can overestimate the damage, since the highest loadings at the beginning (i.e. before the smoothing effect of wear) tends to be over represented.

A linear Palmgren-Miner rule is used at each integration point, so that increment of damage at step i is:

$$\Delta D_i = \frac{\Delta N_c}{N_f(\sigma_{SWT}(i))} \quad (29)$$

where $N_f(\sigma_{SWT}(i))$ is the number of cycles to failure for the corresponding load level $\sigma_{SWT}(i)$. The cumulated damage at step k is obtained with a sum of all increments:

$$D_k = \sum_{i=1}^{k} \frac{\Delta N_c}{N_f(i)} \quad (30)$$

A key issue to apply such cumulative damage law consists in identifying the material endurance relationship $N_f = g(\sigma_{SWT,\ell_d})$. Arnaud and Fouvry [14] suggested to extract a crack nucleation law from plain fretting tests, and added a crack propagation law. Alternatively Said et al [39] suggests to calibrate the material endurance law directly from the fretting fatigue endurance applying the critical distance method so that plotting the N_f endurance as a function of the σ_{SWT,ℓ_d} value. We adopt this latter strategy focusing on partial slip results. Figure 23 plots the $(N_f; \sigma_{SWT,\ell_d})$ results for series A under partial slip, series B and series C. It is interesting to note that all the test conditions with a fatigue stress amplitude higher than 100 MPa tend to follow a master endurance curve. It can be formalized using a Strohmeyer like formulation:

$$log(N_f) = m \cdot \left(log(A) - log\left(\sigma_{SWT,\ell_d} - \sigma_D\right)\right) \quad (31)$$

where $m \simeq 0.38$, $log(A) \simeq 16.2$.

This material law will be considered to simulate the cumulated damage under gross slip.

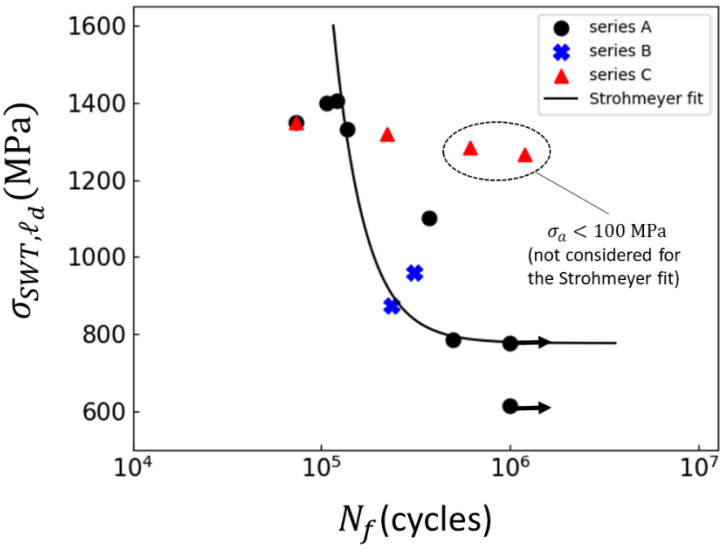

Figure 23: evolution of N_f versus σ_{SWT,ℓ_d} for partial slip conditions (Table 2)

Alternatively, when the fatigue stress amplitude is too low (i.e. $\sigma_a < 100\,MPa$), the endurance doesn't follow anymore the master curve. In fact, the given endurance law is based on a crack nucleation SWT fatigue stress analysis which is reliable only if the propagation stage is short comparatively to the crack nucleation period. This is true as long as the fatigue stress amplitude is high enough. For very low fatigue stress amplitude, the propagation stage is predominant and the given SWT model is no more relevant.

4.3. Validation of the model

4.3.1. Elastic material hypothesis

The model has been developed assuming a perfectly elastic material. However, the large contact forces could induce plasticity. To verify this assumption, two partial slip fretting fatigue tests were simulated: one for the lowest Q^* value ($Q^* = 88\,N$, corresponding to $\delta^* = 9\,\mu m$) and one for the highest ($Q^* = 1090\,N$, corresponding to $\delta^* = 145\,\mu m$). Note that these two simulations have been performed taking into account the corresponding fretting scar dimensions. Figure 24 shows that σ_{Mises} is inferior to $\sigma_Y = 1800\,N$ everywhere for the test at $Q^* = 1090\,N$, so there is no plasticity; but for $Q^* = 88\,N$, σ_{Mises} is superior to σ_Y in a large domain below the contact. This surprising tendency can be explained by the fact that for the very low tangential forces (i.e. $Q^* = 88\,N$), the transient wear is negligible and the contact area remains nearly unchanged. Alternatively, for the highest tangential force amplitudes (i.e. $Q^* = 1090\,N$), the transient wear is significant as well as the corresponding contact area extension so that field stresses are significantly reduced.

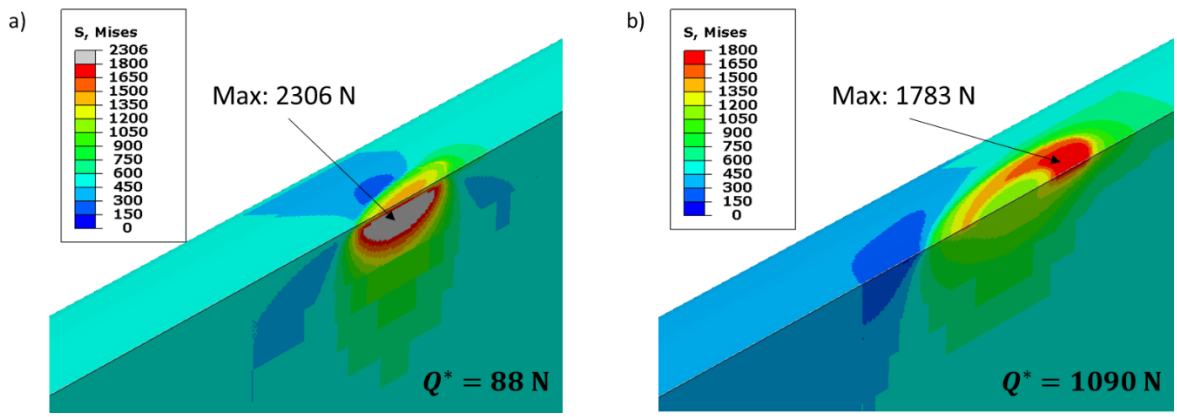

Figure 24: simulations of partial slip fretting fatigue tests at a) $\delta^* = 9$ µm (so $Q^* = 88$ N) and b) $\delta^* = 145$ µm (so $Q^* = 1090$ N), with same fatigue and normal forces ($\sigma_m = 320$ MPa, $\sigma_a = 160$ MPa, $P = 1400$ N)

To evaluate the potential effect of plasticity on crack initiation prediction, the σ_{SWT} subsurface stress field of the most critical situation ($Q^* = 88$ N) was computed using a perfectly plastic law (i.e. with no strain hardening). This stress field has then been compared to the stresses obtained with an elastic formulation. Figure 25 plots the absolute difference of the corresponding σ_{SWT} stresses: $|\Delta\sigma_{SWT}| = |\sigma_{SWT}(E) - \sigma_{SWT}(EP)|$. The difference at the SWT hotspot (close to the trailing edge) where the crack initiation process takes place and at the critical distance under the hotspot is less than 10 MPa. Hence, even if plasticity is occuring, its influence on the crack nucleation at the contact border appears negligible so that the elastic assumption can be considered as relevant.

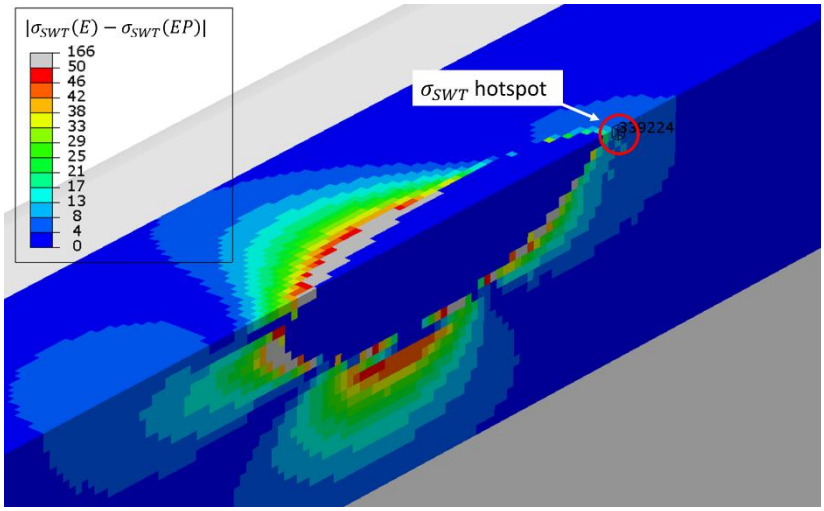

Figure 25: comparison between elastic and elasto-plastic models for test at $Q^* = 88$ N , absolute difference of σ_{SWT} for elastic and elasto-plastic models

4.3.2. Comparison with a “full numerical” model

The “hybrid” model was developed primarily to easily take into account the worn contact geometry evolution. An additional interesting effect is the elimination of FEM contact solving problem, which is particularly computationally expensive. In order to quantify the computation time reduction, a “full numerical” model of two crossed cylinders in contact was built (see Figure 26.a), with friction coefficient $\mu = 0.9$. A normal force $P = 1400$ N and a cyclic tangential force of amplitude $Q^* = 500$ N were applied. Figure 26.b displays the resulting Mises stresses on the surface of the lower wire. The corresponding hybrid model was built, with contact ellipse dimensions calculated using Hertz theory, applying results from Antoine et al. [41]. Since the full numerical model cannot simulate wear, the comparison is done for an undamaged contact. The meshes of both models are exactly the same. Figure 26.c displays a superposition of the Von Mises stresses for both models, along a path indicated at the surface. The difference between the models is negligible, confirming the capacity of the hybrid strategy to simulate 3D fretting fatigue problems. Furthermore, there is a dramatic decrease (factor 10) in the computation time, from 7010 s for the “full numerical” model to 770 s for the hybrid model, with 32 cpus.

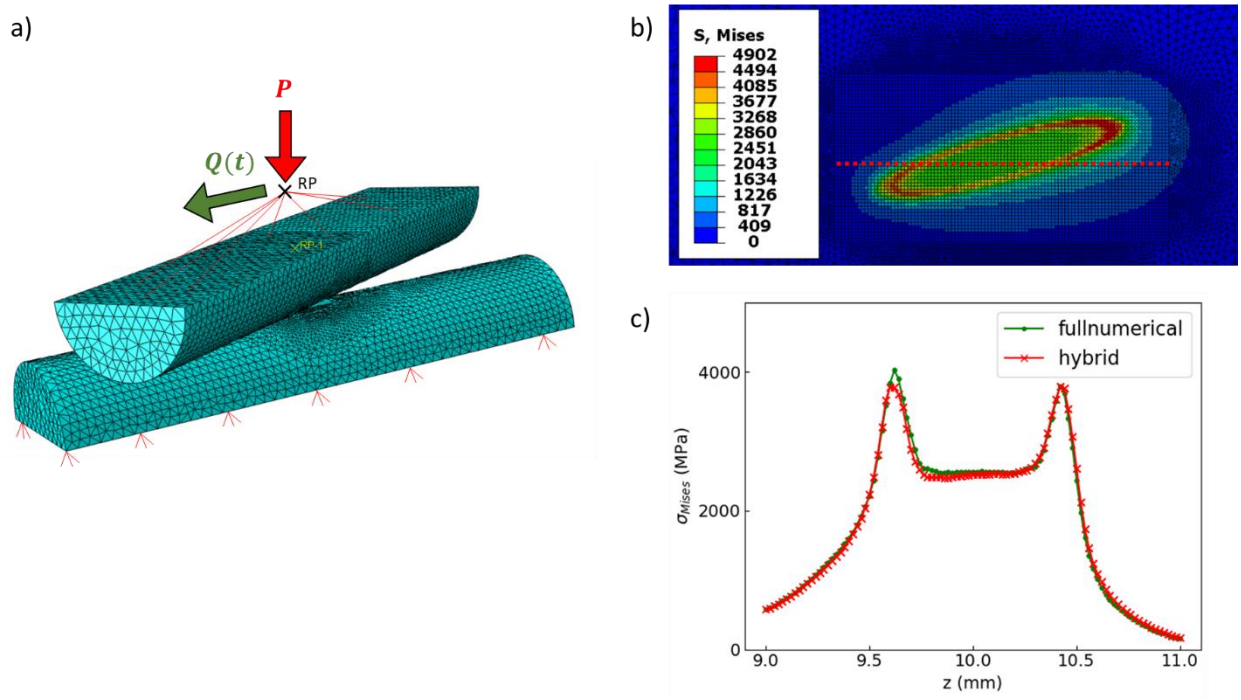

Figure 26: a) “full numerical” model loads b) Von Mises stresses on the “full numerical” model, c) comparison of the Von Mises stresses of both models along a path on the surface

5. Prediction of the fretting fatigue endurance as a function of δ^*

The model is now applied to predict the fretting fatigue endurance as a function of the displacement amplitude from partial to gross slip conditions.

Under partial slip conditions, the tangential force amplitude can be extrapolated from the applied displacement amplitude:

$$Q^* = K_{FF} \cdot \delta^* \quad (32)$$

With K_{FF} being the fretting fatigue stiffness of the experiment including the contact but also the apparatus stiffness (i.e. $K_{FF} = 7.5$ N/µm).

Knowing Q^*, the contact geometry is adjusted applying the empirical relationship (9). The surface wear is supposed instantaneous (i.e. short transient period) so no cumulated wear contact extension effect needs to be considered. Then, using the hybrid contact simulation, the SWT stress field at the critical distance is computed $\sigma_{SWT,\ell_d}(Q^*)$. Knowing $\sigma_{SWT,\ell_d}(Q^*)$, the corresponding fretting fatigue endurance is finally estimated applying equation (31).

Under gross slip condition, the surface wear is continuous and depends on the applied sliding amplitude. Hence, for each δ^*, the sliding amplitude δ_s^* is extrapolated using equation (1). The Archard work is computed $\sum W$ for each δ^* and test duration N_c. From the Archard work the wear volume V is estimated (equation (12)), from which the contact geometry parameters a_X and a_Y are derived, and then the pressure and shear stress elliptical approximation profiles.

For each increment of wear, the SWT equivalent stress at the critical distance is computed and the cumulated damage is estimated. Figure 27 displays the evolution of the maximum value of $\sigma_{SWT,\ell_d}(\delta^*)$ for a $\delta^* = 165\,\mu m$ gross slip amplitude as a function of the surface wear extension. σ_{SWT,ℓ_d} drops fast during the first thousands cycles due to the fast rising of the contact area. σ_{SWT,ℓ_d} decreases asymptotically until passing below the fatigue limit, above 50 000 loading cycles. If the increment of damage becomes null before the cumulated damage reaches 100%, then there should be no failure. Note that the increment of damage becomes null even before σ_{SWT} decreases below σ_D, as wear shifts the hotspot position. Once stable, the maximum damage does not change anymore. Note that the continuous wear not only increases the contact area, but also removes the cracked material before the cracks can propagate, which should lead to a decrease of the maximum damage value in the specimen. This model does not natively take this effect into account. This could be roughly implemented in the model, by deactivating the integration points entering the wear volume. But here, even without taking into account this beneficial effect, the model accurately predicts no failure (as the final damage is inferior to 100%). As no failure is predicted for the lowest gross slip amplitudes, there will be no failure for the larger ones.

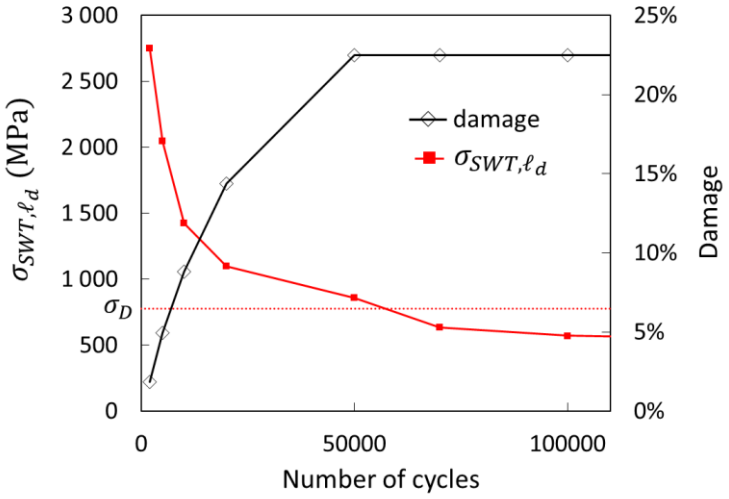

Figure 27: σ_{SWT,ℓ_d} and cumulated damage as a function of the number of cycles, simulation of a fretting fatigue test in gross slip regime ($\delta^* = 165$ µm, $\sigma_m = 320$ MPa, $\sigma_a = 160$ MPa, $P = 1400$ N)

Both fretting fatigue endurance $N_{f,pred}$ predicted under partial and gross slip conditions are computed and compared versus experiments in Figure 28.

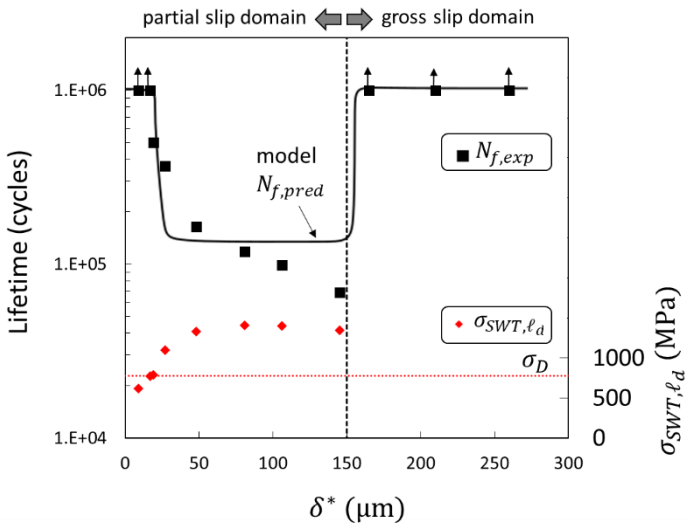

Figure 28: evolution of fretting fatigue endurance as a function of the effective displacement amplitude and correlation with SWT equivalent stress for tests in partial slip. Fatigue load and normal force are kept constant ($\sigma_m = 320$ MPa, $\sigma_a = 160$ MPa, $P = 1400$ N)

A rather nice correlation is observed which confirms the stability of the proposal. The sharp decrease of N_f at the beginning of the partial slip domain: 10 µm $< \delta^* <$ 50 µm as well as the following smoother decrease until the gross slip transition but also the sharp rising up to the "infinite" lifetime under gross slip condition are well depicted. One can explain the coherence of such prediction since the material fatigue endurance was extracted from the post processing of the fretting fatigue endurance under partial slip. However, it must be noticed that this material law endurance is also consistent with endurance values extracted from various fretting fatigue loading conditions (i.e. series B and C) as long as the fatigue stress amplitude is sufficient to neglect the propagation contribution and could be considered as relevant.

Another way to illustrate the capacity of the model to capture the fretting fatigue endurance consists in comparing the evolution of $\sigma_{SWT,\ell_d}(Q^*)$ under partial slip condition. Again, a rather good correlation is observed. σ_{SWT,ℓ_d} remains below σ_D below $\delta^* = 17\ \mu m$, which is consistent with the "no-damage conditions" (i.e. infinite lifetime) observed for the very small displacement amplitude conditions. Then, a fast rising of σ_{SWT,ℓ_d} is observed which is also consistent with the very fast drop of N_f. Then, with the rising of partial slip surface wear, σ_{SWT,ℓ_d} displays a constant value, inducing constant predicted lifetimes in the medium partial slip domain up to the gross slip transition. In contrast, the experimental results show a continuous decrease in lifetime.

As detailed previously, an increase of the displacement amplitude under partial slip increases the tangential loading which is negative regarding cracking. However in the meantime, this extends the contact area during the transient gross slip period which is positive regarding cracking. The flat evolution of the predicted endurances suggests that these two effects are

equally balanced in the given model. The decrease of the experimental endurance infers that the model overestimates the benefit induced by the wear contact area extension. This could be explained by various hypotheses. The model considers smooth elliptical pressure distribution without considering any discontinuous pic pressure induced for instance by the presence of the stick domain and above all the accumulation of debris layer entrapped within the interface [14]. Besides the model does not consider explicitly the propagation stage which indirectly decays the lifetime prediction.

This approach has been generalized by plotting the corresponding fretting fatigue chart Figure 29. The fretting fatigue chart consists in plotting no damage, cracking and wear domains as a function of the applied displacement amplitude ratio δ^*/δ_t^* and the fatigue stress amplitude σ_a. First introduced for plain partial slip conditions in [42], it was extended to gross slip conditions by Arnaud et al in [14]. However, all these developments have been performed for 2D cylinder plane contact. This approach adresses 3D contact configuration thanks to the given hybrid fretting fatigue modelling.

Using this approach, both cracking boundaries under partial and gross slip conditions can be simulated and compared with experiments. As expected, the cracking boundary under gross slip corresponds in fact to the gross slip transition $\delta^*/\delta_t^* = 1$ since the surface wear induces a very fast decrease of the cracking damage (Figure 28). The crack nucleation boundary under partial slip reaches $\delta^*/\delta_t^* \simeq 0.2$ when $\sigma_a = 0$ which in fact corresponds to the crack nucleation threshold under plain fretting loadings on pre-stressed specimen at $\sigma_m = 320$ MPa. Note that the given model does not simulate the crack propagation neither the crack arrest situation. Therefore, some situations predicted as crack failure could in fact correspond to the unfailing crack arrest configuration. Further developments are now required to implement these latter crack arrest/crack propagation concepts to update this 3D fretting fatigue mapping analysis.

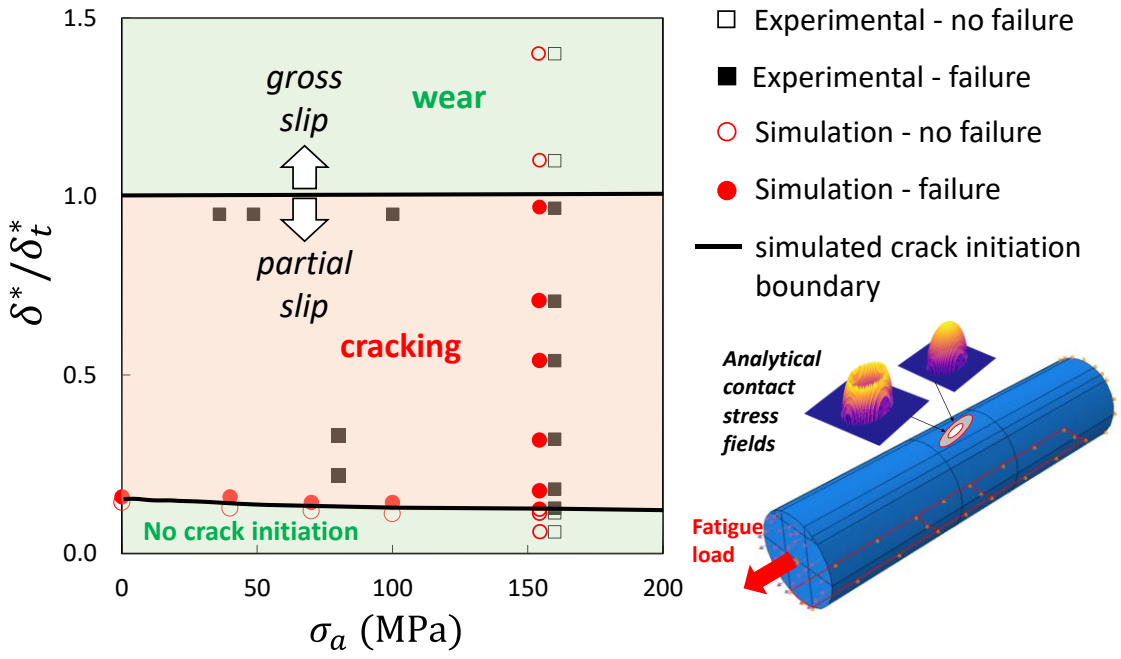

Figure 29: fretting fatigue map. Experimental results and crack initiation boundaries obtained with the model.

Conclusion

In this paper, the effect of contact geometry modifications on fretting fatigue damage was investigated, both in partial and gross slip regimes. Fretting fatigue tests were conducted on crossed steel wires. A double actuator fretting fatigue test machine was used, allowing to keep the fatigue load constant while changing the fretting load. In the partial slip domain, lifetime is over 10^6 cycles for very small fretting loads, and drops to about 10^5 cycles in most of the partial slip domain. In gross slip domain, lifetime is also over 10^6 cycles. Indeed, wear continuously increases the contact interface, thus reducing the contact stresses. In the partial slip domain, there is no continuous wear. However, the wear damage during a short gross slip transition period generates an initial contact area extension.

In order to take into account this partial slip contact area extension, as well as simulate wear in gross slip, a hybrid analytical-numerical model was developed. It is based on the direct application of analytically obtained pressure and shear fields to a FEM model. This method provides a computationally efficient and flexible way to take into account contact geometry modifications, both in partial slip and gross slip regimes. While it is less precise than the traditional continuous remeshing method, it is simpler to implement and much less computationally expensive. Furthermore, the complete decoupling between geometry and

fretting loads allows for a flexible way to explore the effects of different loads. A Smith-Watson-Topper (SWT) approach combined with cumulative damage was implemented on this hybrid model to predict experimental fretting fatigue failures.

Acknowledgments

The authors would like to thank the people at the ArcelorMittal factory of Bourg-en-Bresse for providing the wires.

References

1 Suh, J.-I., & Chang, S. P. Experimental study on fatigue behaviour of wire ropes. International Journal of Fatigue, 9. (2000), p. 339-347. https://doi.org/10.1016/S0142-1123(00)00003-7

2 Gourmelon, J. (2002). Fatigue of staying cables, Organisation and results of the research programme. International Organisation for the Study of the Endurance of Ropes. OIPEEC, Bulletin, 21–39.

3 Nowell, D., Dini, D., & Hills, D. A., Recent developments in the understanding of fretting fatigue, Engineering Fracture Mechanics, 73(2), 2006, p.207–222. https://doi.org/10.1016/j.engfracmech.2005.01.013

4 Wang, D., Zhang, D., & Ge, S. (2011). Fretting–fatigue behavior of steel wires in low cycle fatigue. Materials & Design, 32(10), 4986–4993. https://doi.org/10.1016/j.matdes.2011.06.037

5 Waterhouse, R. B. (2002). Fretting in steel ropes and cables - A review. ASTM Special Technical Publication, 1425, 3–14.

6 Hobbs, R. E., & Raoof, M. (1994). Mechanism of fretting fatigue in steel cables. International Journal of Fatigue, 16(4), 273–280. https://doi.org/10.1016/0142-1123(94)90341-7

7 Raoof, M. (1990). Free Bending of Spiral Strands. Journal of Engineering Mechanics, 116(3). https://doi.org/10.1061/(ASCE)0733-9399(1990)116:3(512)

8 Raoof, M. (1990). Axial Fatigue of Multilayered Strands. Journal of Engineering Mechanics, 116(10). https://doi.org/10.1061/(ASCE)0733-9399(1990)116:10(2083)

9 Raoof, M., & Hobbs, R. E. (1988). Analysis of Multilayered Structural Strands. Journal of Engineering Mechanics, 114(7). https://doi.org/10.1061/(ASCE)0733-9399(1988)114:7(1166)

10 Cruzado, A., Urchegui, M. A., & Gómez, X. (2014). Finite element modeling of fretting wear scars in the thin steel wires: Application in crossed cylinder arrangements. Wear, 318(1), 98–105. https://doi.org/10.1016/j.wear.2014.06.019

11 Fouvry, S., Paulin, C., & Liskiewicz, T. (2007). Application of an energy wear approach to 10quantify fretting contact durability: Introduction of a wear energy capacity concept. Tribology International, 40(10), 1428–1440. https://doi.org/10.1016/j.triboint.2007.02.011

12 McColl, I. R., Ding, J., & Leen, S. B. (2004). Finite element simulation and experimental validation of fretting wear. Wear, 256(11), 1114–1127. https://doi.org/10.1016/j.wear.2003.07.001

13 Madge, J. J., Leen, S. B., McColl, I. R., & Shipway, P. H. (2007). Contact-evolution based prediction of fretting fatigue life: Effect of slip amplitude. Wear, 262(9–10), 1159–1170. https://doi.org/10.1016/j.wear.2006.11.004

14 Arnaud, P., & Fouvry, S. (2020). Modeling the fretting fatigue endurance from partial to gross slip: The effect of debris layer. Tribology International, 143, 106069. https://doi.org/10.1016/j.triboint.2019.106069

15 Gallego, L., & Nélias, D. (2007). Modeling of Fretting Wear Under Gross Slip and Partial Slip Conditions. Journal of Tribology, 129(3), 528–535. https://doi.org/10.1115/1.2736436

16 Done, V., Kesavan, D., Krishna R, M., Chaise, T., & Nelias, D. (2017). Semi analytical fretting wear simulation including wear debris. Tribology International, 109, 1–9. https://doi.org/10.1016/j.triboint.2016.12.012

17 Garcin, S., Baydoun, S., Arnaud, P., & Fouvry, S. (2022). Fretting wear modeling of 3D and 2D Hertzian contacts with a third-body layer using a Winkler elastic foundation model. Tribology International, 170, 107493. https://doi.org/10.1016/j.triboint.2022.107493

18 Fouvry, S., Kapsa, P., & Vincent, L. (1996). Quantification of fretting damage. Wear, 200(1), 186–205. https://doi.org/10.1016/S0043-1648(96)07306-1

19 Jin, O., & Mall, S. (2004). Effects of slip on fretting behavior: experiments and analyses. Wear, 256(7), 671–684. https://doi.org/10.1016/S0043-1648(03)00510-6

20 Vingsbo, O., & Söderberg, S. (1988). On fretting maps. Wear, 126(2), 131–147. https://doi.org/10.1016/0043-1648(88)90134-2

21 Fouvry, S., Duó, P., & Perruchaut, Ph. (2004). A quantitative approach of Ti–6Al–4V fretting damage: friction, wear and crack nucleation. Wear, 257(9), 916–929. https://doi.org/10.1016/j.wear.2004.05.011

22 Mindlin, R. D. (1949). Compliance of Elastic Bodies in Contact. JOURNAL OF APPLIED MECHANICS, 10. https://doi.org/10.1115/1.4009973

23 Johnson, K. L. (1985). Contact mechanics. Cambridge: Cambridge University Press. https://doi.org/10.1017/CBO9781139171731

24 Zhou, Z. R., Fayeulle, S., & Vincent, L. (1992). Cracking behaviour of various aluminium alloys during fretting wear. Wear, 155(2), 317–330. https://doi.org/10.1016/0043-1648(92)90091-L

25 Fouvry, S., Kapsa, Ph., & Vincent, L. (1995). Analysis of sliding behaviour for fretting loadings: determination of transition criteria. Wear, 185(1), 35–46. https://doi.org/10.1016/0043-1648(94)06582-9

26 S. Fouvry, Ph. Kapsa, L. Vincent, “Developments of fretting sliding criteria to quantify the local friction coefficient evolution under partial slip condition”, Tribology Series, Vol. 34, 1998, pp. 161-172.

27 Archard, J. F., & Hirst, W. (1956). The wear of metals under unlubricated conditions. Proceedings of the Royal Society of London. Series A. Mathematical and Physical Sciences, 236(1206), 397–410. https://doi.org/10.1098/rspa.1956.0144

28 Cattaneo, C. (n.d.). Sul contatto di due Corpi Elastici : distribuzione locale degli sforzi. Academia dei Lincei, Rendiconti, 27(6), 342_348, 434–436, 474–478.

29 Proudhon, H., Fouvry, S., Buffière, J.-Y. (2005). A fretting crack initiation prediction taking into account the surface roughness and the crack nucleation process volume. International Journal of Fatigue, 27(5), 569–579. https://doi.org/10.1016/j.ijfatigue.2004.09.001

30 Fouvry S., Liskiewicz T., Paulin C., A global–local wear approach to quantify the contact endurance under reciprocating-fretting sliding conditions, Wear, Volume 263, Issues 1-6, 10, 2007, Pages 518-531.

31 Deresiewicz, H. (1957). Oblique contact of nonspherical elastic bodies. Journal of Applied Mechanics, (24), 623–624. https://doi.org/10.1115/1.4011612

32 Nowell, D., & Hills, D. A. (1987). Mechanics of fretting fatigue tests. International Journal of Mechanical Sciences, 29(5), 355–365. https://doi.org/10.1016/0020-7403(87)90117-2

33 Smith, K. N., Topper, T., & Watson, P. (1970). A stress–strain function for the fatigue of metals (stress-strain function for metal fatigue including mean stress effect). J Materials, 5, 767–778.

34 Proudhon, H., Fouvry, S., & Yantio, G. (2006). Determination and prediction of the fretting crack initiation: introduction of the (P, Q, N) representation and definition of a variable process volume. https://doi.org/DOI: 10.1016/j.ijfatigue.2005.09.005

35 Szolwinski, M. P., & Farris, T. N. (1996). Mechanics of fretting fatigue crack formation. Wear, 198(1), 93–107. https://doi.org/10.1016/0043-1648(96)06937-2

36 Amargier, R., Fouvry, S., Chambon, L., Schwob, C., & Poupon, C. (2010). Stress gradient effect on crack initiation in fretting using a multiaxial fatigue framework. International Journal of Fatigue, 32(12), 1904–1912. https://doi.org/10.1016/j.ijfatigue.2010.06.004

37 Araújo, J. A., Susmel, L., Taylor, D., Ferro, J. C. T., & Mamiya, E. N. (2007). On the use of the Theory of Critical Distances and the Modified Wöhler Curve Method to estimate fretting fatigue strength of cylindrical contacts. International Journal of Fatigue, 29(1), 95–107. https://doi.org/10.1016/j.ijfatigue.2006.02.041

38 Taylor, D. (1999). Geometrical effects in fatigue: a unifying theoretical model. International Journal of Fatigue, 21(5), 413–420. https://doi.org/10.1016/S0142-1123(99)00007-9

39 Said, J., Fouvry, S., Cailletaud, G., Basseville, S., Coulangeon, M., Brocard, J., … Hafid, F. (2023). A global-local approach to predict the fretting-fatigue failure of clamped aluminum powerline conductors: from mono-contact crossed wires to full conductor vibrational tests. Engineering Failure Analysis, 107073. https://doi.org/10.1016/j.engfailanal.2023.107073

40 Paulin, C., Fouvry, S., & Meunier, C. (2008). Finite element modelling of fretting wear surface evolution: Application to a Ti–6A1–4V contact. Wear, 264(1), 26–36. https://doi.org/10.1016/j.wear.2007.01.037

41 Antoine, J.-F., Visa, C., Sauvey, C., & Abba, G. (2006). Approximate Analytical Model for Hertzian Elliptical Contact Problems. Journal of Tribology, 128(3), 660. https://doi.org/10.1115/1.2197850

42 Fouvry, S., Kubiak, K. (2009). Introduction of a fretting-fatigue mapping concept: Development of a dual crack nucleation – crack propagation approach to formalize fretting-fatigue damage. International Journal of Fatigue, 31(2), 250–262. https://doi.org/10.1016/j.ijfatigue.2008.09.002